JACS
JOURNAL OF THE AMERICAN CHEMICAL SOCIETY
pubs.acs.org/JACS
Article

Heterolytic C–H Activation Routes in Catalytic Dehydrogenation of Light Alkanes on Lewis Acid–Base Pairs at ZrO_2 Surfaces

Nicholas R. Jaegers, Vardan Danghyan, Junnan Shangguan, Carlos Lizandara-Pueyo, Prashant Deshlahra, and Enrique Iglesia*

Cite This: J. Am. Chem. Soc. 2024, 146, 25710–25726
Read Online

ABSTRACT: Alkane dehydrogenation is an enabling route to make alkenes useful as chemical intermediates. This study demonstrates the high reactivity of Lewis acid–base (LAB) site pairs at ZrO_2 powders for dehydrogenation of C_2–C_4 alkanes and the essential requirement for chemical treatments to remove strongly bound H_2O and CO_2 titrants to avoid the high temperatures required for their desorption and the concomitant loss of active sites through sintering and annealing of ZrO_2 crystallites. The energies and free energies of bound intermediates and transition states from density functional theory (DFT), taken together with kinetic analysis and isotopic methods, demonstrated the kinetic relevance and heterolytic character of the first C–H activation at terminal C-atoms for all alkanes with a modest activation barrier (84 kJ mol^{-1}) at essentially bare Zr–O LAB site pairs. β-Hydride elimination from the formed alkyl carbanions lead to their desorption as alkene products in steps that are favored over their parallel C–C cleavage reactions (by 100 kJ mol^{-1}), leading to high dehydrogenation selectivities (>98%) at the temperatures required for practical yields in such endothermic dehydrogenation reactions (700–900 K). The facile recombination of bound proton-hydride pairs then completes a dehydrogenation turnover. These findings provide compelling evidence for the remarkable reactivity and selectivity of LAB sites on earth-abundant oxides and for the need to uncover them through chemical treatments, which combine to give gravimetric dehydrogenation rates that exceed those on the toxic (Cr) or costly (Pt) catalysts used in practice.

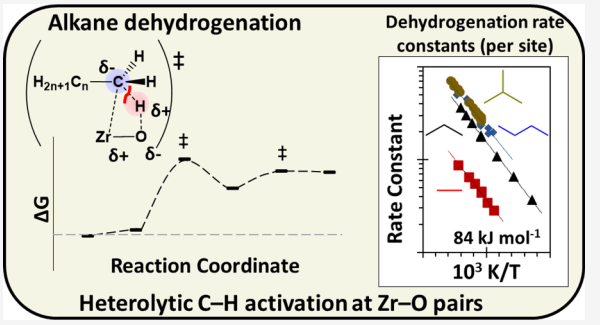

1. INTRODUCTION

Light alkenes are essential feedstocks for the synthesis of chemical intermediates. They are produced through thermal cracking of natural gas condensate and naphtha feedstocks and as a side product of catalytic cracking of petroleum-derived streams. The emergence of shale gas as a carbon feedstock led to an abundance of propane, but the use of its condensate fraction in thermal cracking favors C_2H_4 over C_3H_6 as products;[1] taken together, these trends have led to renewed emphasis on the production of C_3H_6 via direct on-purpose C_3H_8 dehydrogenation.[2] These processes currently use costly Pt-based catalysts (e.g., Oleflex^{TM})[3] or toxic Cr-based catalysts (e.g., Catofin).[4] These catalytic reactions are proposed to proceed via homolytic C–H activation channels on metal and redox-active centers, although heterolytic pathways have also been proposed on Cr(III) centers.[5] These systems lead to parasitic C–C cleavage reactions and to unsaturated organic residues, which cause, in turn, alkene yield losses and catalyst deactivation.[6]

Surfaces of earth-abundant oxides, and specifically their exposed Lewis acid–base (LAB) pairs, can activate C–H bonds in alkanes and alkanols.[7−11] ZrO_2 catalysts activate C–H bonds in oxygenates via heterolytic routes on exposed $Zr^{\delta+}$–$O^{\delta-}$ site pairs,[12] with a kinetic competence that depends on the identity of the ZrO_2 crystal phase and the exposed surface facets.[13,14] These LAB centers also activate the H–OH bonds of H_2O[15,16] in very exothermic reactions (−140 to −165 kJ mol^{-1}) to form strongly bound H^+–OH^- pairs.[15,17] Consequently, H_2O titrates LAB sites, rendering them inaccessible for catalysis and obscuring their high intrinsic reactivity in C–H activation steps. These H_2O (and e.g., CO_2) titrants can be desorbed from LAB sites by thermal treatments, but at temperatures that cause sintering and annealing, which leads to the destruction of the low-coordination sites that are most competent in stabilizing H_2O dissociation products and C–H activation transition states.

The uncovering of low-coordination sites at ZrO_2 surfaces by chemical treatments circumvents these obstacles and leads to gravimetric alkane dehydrogenation rates similar to (and

Received: June 10, 2024
Revised: August 24, 2024
Accepted: August 26, 2024
Published: September 6, 2024

https://doi.org/10.1021/jacs.4c07766
J. Am. Chem. Soc. 2024, 146, 25710–25726

even higher than) those on Pt and Cr catalysts. Dimethyl ether, as well as CH_3OH and alkenes, react with bound species derived from H_2O and CO_2 to uncover LAB sites at much lower temperatures than thermal treatments intended to desorb titrants, leading to rates about 100-fold higher than on catalysts treated in He, H_2, or O_2.[18,19] Such unique reactivity is preserved during alkane dehydrogenation catalysis only through the strict removal of H_2O and CO_2 (and any molecule, such as O_2, that forms them) from inlet streams.[18,19]

This study exploits these chemical treatments and the use of anhydrous and anerobic inlet streams to assess the properties of uniquely active Zr−O LAB site pairs and the mechanistic details of the heterolytic C−H activation routes that they mediate in the dehydrogenation of C_2-C_4 alkanes. The evidence provided shows that the chemical treatments that activate ZrO_2 catalysts serve as chemical desiccants that remove H_2O-derived titrants from the active sites, thus enabling detailed mechanistic assessments of alkane dehydrogenation on clean Zr−O site pairs. In contrast to homolytic alkane dehydrogenation routes, these heterolytic channels enable C−H cleavage without the formation of radical-like species or the formation/involvement of reduced Zr atoms as active centers, a requirement invoked in previous studies.[20] These reactions of C_2-C_4 alkanes proceed through kinetically relevant C−H abstraction transition states (TS) and their relative reactivities reflect differences in activation entropies resulting from the greater retention of molecular mobility for larger bound anionic alkyls at the C−H activation TS. DFT-derived energies of bound intermediates and transition states confirmed the common kinetically relevant steps among these alkanes and the requirement for realistic structural models of low-coordination Zr−O pairs at plane intersections in nanoparticle surfaces for even more accurate theoretical descriptions. DFT-based assessments, combined with kinetic trends and isotope effects, also confirmed the essentially bare nature of Zr−O pairs during alkane dehydrogenation catalysis, in agreement with measured rates that are strictly proportional to C_2-C_4 alkane pressures.

2. EXPERIMENTAL AND COMPUTATIONAL METHODS

2.1. Catalyst Synthesis. ZrO_2 samples were prepared by a known hydrothermal method.[21] $ZrO(NO_3)_2{\cdot}xH_2O$ (Sigma-Aldrich, 99%, 12.7 g) and $CO(NH_2)_2$ (urea; Sigma-Aldrich, 99.5%; 21.6 g) were separately dissolved in 30 cm^3 H_2O (18.2 MΩ·cm) at 323 K. The solutions were mixed, placed in a Teflon-lined autoclave, and held at 393 K for 20 h; $CO(NH_2)_2$ decomposed during this process, leading to a gradual increase in pH and to the precipitation of Zr oxyhydroxides. The powders formed were suspended in H_2O (18.2 MΩ·cm) and separated by centrifugation (8000 rpm), a sequence repeated four times. They were then treated in ambient stagnant air at 393 K for 12 h. Next, the samples were heated in flowing He (Praxair, 99.999%, 1.6 cm^3 g^{-1} s^{-1}) at 723 K (0.17 K s^{-1}) for 5 h. These procedures formed the monoclinic phase of ZrO_2 (*m*-ZrO_2), as shown from measured diffractograms and reference patterns (Figure S1). Its BET surface area was 130 m^2 g^{-1}, as measured by N_2 physisorption (described in the Supporting Information section S1). Higher treatment temperatures cause sintering and a loss of surface area (from 130 m^2 g^{-1} at 723 K to 110 m^2 g^{-1} after treatment at 873 K). Another *m*-ZrO_2 sample was obtained from commercial sources (NORPRO; Saint-Gobain) and treated in flowing He (Praxair, 99.999%, 1.6 cm^3 g^{-1} s^{-1}) by heating to 723 at 0.17 K s^{-1} and holding for 5 h. This sample showed a surface area of 112 m^2 g^{-1} and X-ray diffractograms confirmed its monoclinic crystal structure. These samples and the inert diluents used in all catalytic experiments were sieved to retain 180−250 μm aggregates before use.

2.2. Chemical Treatments and Alkane Dehydrogenation Rate Measurements. Alkane dehydrogenation rates were measured on ZrO_2 catalysts (0.02−0.1 g) using either straight or U-shaped quartz tubular reactors (1 cm internal diameter). Catalyst aggregates were mixed with quartz powders (Sigma-Aldrich, 180−250 μm; treated in 1 M HNO_3 at 293 K for 1 h, washed with 18.2 MΩ-cm H_2O, and then heated to 1073 K in flowing dry air at 10 K min^{-1} and held for 8 h). Dilution ratios (by mass) were >20:1 quartz/ZrO_2 (typically 50:1), a dilution extent shown to avoid reaction-induced temperature changes. Reactors containing catalyst samples were resistively heated (Applied Test Systems 3210 series furnace); temperatures were set by a Watlow 96 controller and measured using a K-type thermocouple in contact with the outer reactor wall at its catalyst bed axial midpoint. Gaseous reactants were metered by using electronic mass flow controllers (Porter).

Catalysts were treated in He flow (Praxair, 99.999%; 40−100 cm^3 g^{-1} s^{-1}) by heating to 723 K at 0.33 K s^{-1} and holding for 1 h before rate measurements. Catalysts were treated using chemical cleansing protocols,[18] unless otherwise noted. These treatments involved exposing samples to dimethyl ether (DME; 1.5 kPa; from Praxair, 5.0% DME, 5.1% Ar in He; 40 cm^3 g^{-1} s^{-1}) for 0.25 h at 723 K and then to a He flow for 0.42 h to remove residual DME and reaction products. In some cases, samples were treated in O_2 to remove carbonaceous deposits that formed after extended use; these treatments involved treatments in O_2 (Praxair, 99.99%, 5% O_2 in He; 40 cm^3 g^{-1} s^{-1}) for 0.5 h at 723−873 K; these treatments led to the full recovery of alkane dehydrogenation rates after subsequent DME treatments.

Rate and selectivity measurements were carried out by flowing different combinations of He, H_2 (Praxair, 99.999%), C_2H_6 (Praxair, 50% in Ar, 99.999%), C_3H_8 (Praxair, 20−50% in Ar, 99.999%), C_3H_6 (Praxair, 49.9% in He, 99.999%), nC_4H_{10} (Praxair, 24.3% in Ar, 99.999%), and iC_4H_{10} (Praxair, 25.2% in Ar, 99.999%) through the catalyst bed. Unless otherwise noted, such reactant mixtures were treated by flowing them through an O_2/H_2O scrubber (Agilent 5182−9401, 5 ppb) located directly upstream of the reactor.

The identity and concentration of all species in the reactor effluent were determined by online gas chromatography (Agilent 6890A GC) using flame ionization detection (FID) after separation in a capillary column (Agilent; HP-1) and thermal conductivity detection (TCD) after separation in a HP-PLOT-Q column. Products were identified in the chromatographs by comparing their retention times to those of chemical standards and from analysis of representative gas samples by mass spectrometry after similar chromatographic protocols (Agilent 6890A equipped with 5975C MS).

Rates were measured over a range of pressures of alkanes (1−30 kPa) and H_2 (0−30 kPa). They are reported as molar rates of formation of the respective product per mass (gravimetric), surface area (areal), or number of active sites (turnover rates, measured by site titration using H_2O; see Supporting Information section S3). Dehydrogenation rates were determined by correcting the measured rates for approach to equilibrium, calculated from the mean reactor gas composition and the equilibrium constant (K_{C-H}) for the dehydrogenation of the respective alkane. K_{C-H} values are shown for a range of temperatures in Figure S3 for C_2H_6, C_3H_8, *n*-C_4H_{10}, and *i*-C_4H_{10} dehydrogenations. Selectivities are reported on a carbon basis as the ratio of converted alkane molecules that formed alkanes to those formed from C−C bond scission events. Contributions from homogeneous reactions were small (<0.2% of catalytic rates) but were nevertheless subtracted from all reported rates and selectivities.

Trace quantities of H_2O and O_2 (which forms H_2O from reactions with H_2 and/or hydrocarbons) titrants, present at about 0.1 ppm even after passage through the O_2-H_2O scrubbers, led to the titration of active sites and to a gradual decrease in dehydrogenation rates with time. These rates were corrected for deactivation by extrapolating forward rates ($r_{f,t}$) using a first-order deactivation equation, eq 1:

$$r_{f,t} = r_0 \, e^{-k_d t} \tag{1}$$

https://doi.org/10.1021/jacs.4c07766
J. Am. Chem. Soc. 2024, 146, 25710−25726

where $r_{f,t}$ is the rate at time t, r_0 is the reaction rate at zero time for the given condition, and k_d is the deactivation rate constant representing active site titration. Such treatments are applicable for early times on stream which show linear rates with time on a semilog plot, or through piecewise application of multiple first-order deactivation models for segments of an experiment in which reaction conditions were changed, thus accounting for the fraction of active sites lost in preceding reaction conditions. Activation barriers for alkane dehydrogenation were also assessed by measuring rates at the highest temperature (e.g., 773 K) and rapidly cooling the catalyst bed. These protocols led to rate and activation energy data that were replicated multiple times in two different reactor systems and for different samples; the agreement between these barriers and those derived from DFT (section 3.5) serves as an independent reassurance of the accuracy and fidelity of these barriers. Rate measurements were taken every 60−120 s to reduce the effects of site deactivation by trace titrant impurities.

C_3H_8-D_2 (Cambridge Isotope Laboratories, Inc., D, 99.8% (D_2, 99.5% + HD, 0.4%)) and C_3H_8-C_3D_8 (Aldrich; propane-d_8, 99 atom% D) mixtures were also used as reactants on m-ZrO_2. The isotopologues formed were determined by collecting the effluent into sample bags and speciating with a mass-selective detector (Agilent, 5957C) after chromatographic separation (HP-1, 50 m × 0.32 mm × 1.05 μm). The relative concentrations of each isotopologue were determined from mass fragmentation patterns using matrix deconvolution methods.[22] The rates of formation of $C_3D_{8-x}H_x$ products were used to measure cross-exchange rates and to determine the reversibility of C−H activation steps by comparing them to propene formation rates.

2.3. Computational Methods. DFT calculations were implemented using the Vienna ab initio simulation package (VASP; version 5.4.4).[23] The generalized gradient approximation (GGA) as prescribed by the Perdew-Burke-Ernzerhof (PBE) method was used to simulate exchange and correlation interactions.[24] The modified dispersion correction (D3) by Grimme et al. was applied to each energy minimization step to account for long-range dispersive interactions.[25] Interactions between core and valence electrons were described using projector-augmented wave pseudopotentials.[26] Valence states of [$4s^24p^64d^25s^2$], [$2s^22p^4$], [$2s^22p^2$], and [$1s^1$] were considered for Zr, O, C, and H atoms, respectively. Plane-wave basis sets were cutoff at 450 eV for all calculations, justified by diminishing changes to structure energy as previously reported.[27] A Monkhorst-Pack[28] k-point 3 × 3 × 1 grid was used to sample the first Brillouin zone. Dipole corrections were used to eliminate long-range electrostatic interactions among the periodic slabs and bound molecules, in the direction perpendicular to the slab surface, as well as among isolated molecules in a vacuum in all directions (used as representative gaseous species). Electronic structures were converged to 10^{-6} eV in self-consistent steps and geometries were converged to 0.05 eV $Å^{-1}$. All calculations were conducted in the spin-polarized mode. The use of a Hubbard correction to account for strongly correlated electrons was considered but not implemented because the nonredox nature of the reaction precludes occupation of Zr 4f states and because it did not detectably affect dissociative adsorption energies of C_3H_8 on m-$ZrO_2(\bar{1}11)$, as also shown in previous work.[20]

Transition state (TS) structures were isolated by first applying the nudged elastic band (NEB) approach[29] and then refined by the Climbing Image method[30] to more accurately determine the saddle point, which was then optimized using the Henkelman Dimer method.[31] The converged TS structures were confirmed by their single imaginary frequency corresponding to the vibration along the reaction coordinate. Vibrational frequencies for surface and gaseous species were calculated using the harmonic oscillator approximation with atomic displacements of ±0.0015 nm. Reported energies are referenced to the relevant structures of a bare surface and a gaseous alkane (or alkene and H_2). A complete description of the methods used to calculate energies is included in the Supporting Information section S7. Briefly, enthalpies were estimated from zero-point vibrational (ZPV) corrections, and vibrational enthalpies were derived from vibrational frequencies. Entropies were derived from statistical mechanics formalisms[32] also using DFT-derived vibrational frequencies. Gibbs free energies were derived from the computed enthalpies and entropies. Vibrational frequencies were calculated using harmonic oscillator formalisms that often fail to accurately describe low frequencies modes,[33] resulting in overestimations in the entropy of surface bound species. These matters were addressed by replacing the contributions from low frequency modes (threshold set at <90 cm^{-1} from visual inspection of vibrational modes from bound C_3H_8 intermediates) with a fraction (0.7) of the corresponding rotational and translational entropy and enthalpy of the gaseous analogs of bound species (i.e., a number (L) vibrational modes < 90 cm^{-1} were replaced with 0.7·L/6 for nonlinear or 0.7·L/5 for linear molecules of the gaseous rotational and translational entropy and enthalpy).[34−36]

Enthalpies (H) were determined using eq 2:

$$H = E_0 + E_{ZPV} + H_{vib} + H_{trans} + H_{rot} \quad (2)$$

where E_0 is the DFT-derived electronic energy, E_{ZPV} is the zero-point vibrational energy, and the H terms reflect the vibrational, translational, and rotational contributions to enthalpy. A complete description of the entropy and free energy computation from statistical thermodynamics treatments[37] is available in eqs S1−S11. All reported enthalpies, free energies, and entropies are reported at a temperature of 723 K, corresponding to typical experimental temperatures reported here for alkane dehydrogenation reactions, unless noted otherwise.

Periodic slab models of m-ZrO_2[38,39] surfaces were generated using 9 × 9 × 6 Monkhorst Pack k-point grids[40] and relaxed lattice constants of a = 0.522 nm, b = 0.528 nm, c = 0.539 nm, which are within 2% of those measured and estimated by theory in previous reports.[17,41−46] The m-ZrO2$(\bar{1}11)$ facet was used as the exposed plane due to its low surface energy.[47−51] The slab model consists of [2 × 2]-supercells and four layers (Zr basis in the c-axis direction) and 1.65 nm vacuum layers between slabs; the bottom two layers of ZrO_2 were kept at their bulk crystallographic positions during all energy and geometry optimizations. The top view of the [2 × 2] supercell surface, visualized with VESTA,[52] is shown in Figure 1. There are four

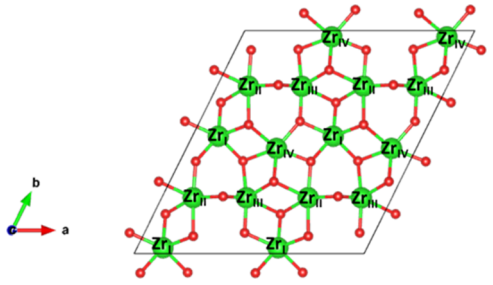

Figure 1. Model of the m-$ZrO_2(\bar{1}11)$ surface.

coordinatively distinct Zr-atoms: Zr_I, Zr_{II}, and Zr_{III} centers are six-coordinate, and Zr_{IV} is seven-coordinate. Unless specified otherwise, computations of adsorbates were conducted on 2.0 Å Zr_{II}−O bond of the 2-coordinate O-atom also bound to Zr_{III}; this Zr−O pair exhibited the strongest dissociative binding energy of H_2O among all pairs surveyed on the surface.

3. RESULTS AND DISCUSSION

3.1. Kinetic Trends in Alkane Dehydrogenation on Chemically Treated m-ZrO_2 Surfaces. Previous studies have shown that high alkane dehydrogenation rates on ZrO_2 surfaces require strictly anhydrous conditions (and the removal of O_2 to < 0.1 ppm, because it forms H_2O and CO_2 during reaction).[19] Treatments that remove bound titrants through chemical reactions lead to rates about 100-fold higher than on samples treated thermally at similar temperatures, because such treatment temperatures are lower than those required for complete desorption.[18] As a result, these chemical dehydrox-

https://doi.org/10.1021/jacs.4c07766
J. Am. Chem. Soc. 2024, 146, 25710−25726

ylation and decarboxylation reactions of ZrO_2 surfaces circumvent the loss of surface area and the preferential destruction of low-coordination Zr−O pairs caused by thermal treatments at temperatures required for desorbing these titrants (e.g., >773 K).

Dimethylether (DME) is particularly effective as a chemical desiccant at modest temperatures (500−723 K) through its hydrolysis[53] or reforming[54] reactions with bound hydroxyl pairs; other reagents (CH_3OH and even alkenes formed from alkane dehydrogenation) are also effective, but in some cases required higher temperatures than DME (e.g., C_3H_6 at 873 K vs DME at 523−723 K). The products detected by online mass-spectrometry are those expected from DME reactions with hydroxyl pairs, specifically reforming and hydrolysis reactions that form CO, H_2, and CH_3OH. Trace H_2O and/or O_2 impurities in the inlet stream stoichiometrically titrate such sites during reaction and lead to a decrease in rates with time during contact with reactant streams. Such rates can be recovered by subsequent DME treatments (Figure S5). After DME cleaning protocols, gravimetric C_3H_8 dehydrogenation rates on *m*-ZrO_2 at 723 K exceed those reported on Cr-based catalysts (Catofin process; Figure S8) at significantly higher temperatures (873 K). Apparent rate constants for C_3H_8 dehydrogenation on DME-treated *m*-ZrO_2 (e.g., 4 mol kg^{-1} h^{-1} kPa^{-1} at 773 K) are also similar or higher than on several reported Pt-based catalysts (used in Oleflex-like processes; e.g., 2.4−15 mol kg^{-1} h^{-1} kPa^{-1} at 873 K; Figure S8).[19,55,56] These earth-abundant ZrO_2-based catalysts avoid the use of costly or toxic elements for the on-purpose synthesis of alkenes via alkane dehydrogenation.

Rate enhancements by DME chemical treatments were previously shown for C_3H_8 reactants on *m*-ZrO_2,[18] but they are also evident for other alkanes (C_2H_6, nC_4H_{10}, and iC_4H_{10}), as shown by the rate data in Figure 2. Dehydrogenation rates

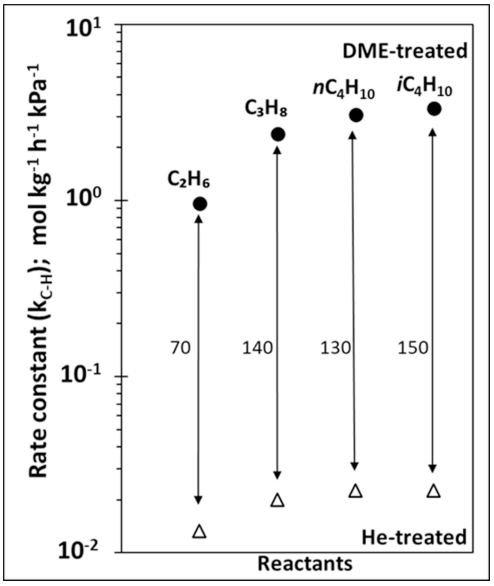

Figure 2. First-order dehydrogenation rate constants (at 723 K) for C_2H_6, C_3H_8, nC_4H_{10}, and iC_4H_{10} reactants after treatment in He (723 K, open triangles) and DME (723 K, black circles). Each rate constant was assessed on the same ZrO_2 sample, testing C_3H_8 before and after each other alkane to ensure that sample quality was retained and measurements were consistent. Rate enhancement by DME treatment for each alkane is listed adjacent to the black double arrows.

increased about 100-fold with these DME treatments over those measured after He treatments at the same temperature (723 K) for each of these alkanes. In the case of nC_4H_{10} reactants, equilibrated mixtures of 1-butene and cis and trans 2-butenes were detected together with low concentrations of 1,3-butadiene.

For all alkanes, forward dehydrogenation rates were proportional to the pressure of the alkane and were unaffected by those of H_2 or alkene products (Figure 3). This first-order

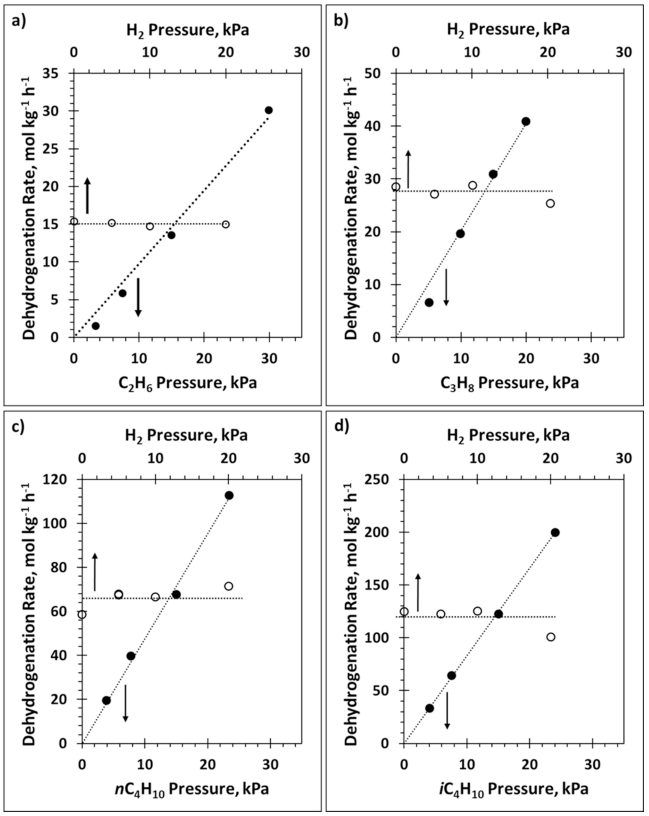

Figure 3. Dehydrogenation rates of a) C_2H_6 (773 K), b) C_3H_8 (723 K), c) nC_4H_{10} (773 K), and d) iC_4H_{10} (773 K) reactants on DME-treated *m*-ZrO_2 as a function of the respective alkane pressure (bottom axis, closed circles) at 5.1 kPa H_2, and of the H_2 pressure (top axis, open circles) at 14−16 kPa alkane. Dashed lines to reflect trends.

relation to alkane pressure was observed for C_3H_8 dehydrogenation up to at least 93 kPa of C_3H_8. The respective first-order rate constants for dehydrogenation of C_2H_6, C_3H_8, nC_4H_{10}, and iC_4H_{10} at 723 K are shown in Figure 2 for samples treated in He or DME at 723 K. These rate constants increased with alkane chain length on samples treated in He at 723 K; these effects of alkane size are weaker than previously reported on *m*-ZrO_2 at 873 K, but similar in trend.[20] These reactant size effects persist after DME chemical treatments, but the rates for all alkanes are significantly higher than those on samples treated in He (~100-fold for C_2-C_4 alkanes). ZrO_2 also effectively dehydrogenates larger alkanes, such as those that are liquid at 300 K and 1 bar (e.g., C_7 alkanes) and DME treatments can be used to enhance these rates. Such larger alkanes also require strict reactant purificaiton protocols;[19] a topic that will be addressed in a future publication.

These trends with alkane size and the effects of chemical treatments on *m*-ZrO_2 samples (130 m^2 g^{-1}) prepared by the

https://doi.org/10.1021/jacs.4c07766
J. Am. Chem. Soc. 2024, 146, 25710−25726

methods described in section 2.1 are also evident on commercial m-ZrO_2 powders (Saint Gobain; 112 m^2 g^{-1}; Figure S4) for which areal rates after DME treatments (185 μmol m^{-2} h^{-1}; 15.2 kPa C_3H_8, 5.1 kPa H_2, and 723 K) were similar to those on the m-ZrO_2 (202 μmol m^{-2} h^{-1}; 15.2 kPa C_3H_8, 5.1 kPa H_2, and 723 K).

The dehydrogenation rate trends with alkane (C_2H_6, C_3H_8, nC_4H_{10}, and iC_4H_{10}) and H_2 pressures on DME-treated m-ZrO_2 are shown in Figure 3 for each alkane. These rates were proportional to the alkane pressure, consistent with kinetically relevant C−H activation steps on Zr−O pairs that remain essentially bare during dehydrogenation turnovers; H_2 did not inhibit forward dehydrogenation rates but can affect rates measured as alkane conversion approaches equilibrium levels, a thermodynamic effect unrelated to the kinetic competence of the Zr−O site pairs. These data show that forward rates of alkane dehydrogenation (r_{C-H}) can be accurately described by the rate equation, eq 3:

$$r_{C-H} = k_{C-H}\cdot[C_nH_{n+2}] = k_BT/h\ e^{-\Delta G^{\ddagger}/RT}\cdot[C_nH_{n+2}] \quad (3)$$

where k_{C-H} is the first-order dehydrogenation rate constant, $[C_nH_{n+2}]$ is the alkane pressure, and $\Delta G^{\ddagger}$ is the free energy of formation of the kinetically relevant C−H activation TS from its relevant precursors (a bare ZrO_2 surface and a gaseous alkane molecule).

The kinetic relevance of C−H activation steps, inferred from rates strictly proportional to the pressure of each alkane, was confirmed for propane reactants by comparing C_3H_8 and C_3D_8 dehydrogenation rates (4 kPa alkane, 5 kPa H_2, and 723 K). These rates were 2.2 times larger for C_3H_8 than C_3D_8, a normal kinetic isotope effect that is consistent with the kinetic relevance of C−H activation, but which remains agnostic about whether the methyl or methylene C−H bond in C_3H_8 is activated in the kinetically relevant step. It also does not discern whether the first or second sequential C−H activation step is the kinetically relevant elementary step. DFT-derived values of the kinetic isotope effects for proton abstraction (from statistical mechanics and vibrational frequencies; see section 3.6) agree with those measured (2.4 vs 2.2), reinforcing the plausibility of the kinetic relevance proton abstraction.

Experiments with C_3H_8-D_2 reactant mixtures were used to infer the extent to which the initial C−H activation step is reversible during dehydrogenation turnovers by comparing the rates of D-incorporation into C_3H_8 reactants and their chemical conversion to propene. Rates of C_3H_8 dehydrogenation on DME-treated m-ZrO_2 were about 5-fold higher than for D-insertion into C_3H_8 (723 K, Figure S6), and D-introduction rates remained constant with time while dehydrogenation rates decreased due to site titration. These results indicate that C−H activation steps do not undergo reverse reactions with D_2 molecules to detectable extents under these conditions (but the alkyl fragment may recombine with the previously abstracted proton before isotopic exchange can occur) and that the deuteration of unreacted propane molecules occurs on sites distinct from those that activate C−H bonds most competently. H_2-D_2 exchange rates on m-ZrO_2 at 723 K (Figure S6) also show that exchange occurs via routes unrelated to those that activate C−H bonds and recombine H-atoms in catalytic dehydrogenation turnovers, evident by a lack of influence of on-stream H_2O pulses (723 K, 0.05−0.25 H_2O·(active site)$^{-1}$) or DME pulses (723 K, 0.3−1 C_2H_6O·(active site)$^{-1}$) on H_2-D_2 exchange rates. This contrasts C_3H_8 dehydrogenation experiments which decrease in proportion to the number of H_2O molecules in each pulse (see Supporting Information section S3).

3.2. Activation Barriers and Their Implications for C−H Activation Routes in C_2-C_4 Alkanes.

Figure 4 shows the first-order dehydrogenation rate constants (per site, measured by H_2O titration methods; rates vs H_2O uptake shown in Supporting Information section S3) in Arrhenius-type form for C_2H_6, C_3H_8, nC_4H_{10}, and iC_4H_{10} reactants on DME-treated m-ZrO_2 (at 723 K). The dehydrogenation rate constants among these alkane reactants reflect site-normalized analogs of the gravimetric rate constants reported in Figure 2 (at 723 K). The activation barriers obtained from rates during decreasing temperature protocols (after chemical treatment and a temperature increase cycle) are listed in Table 1 along with activation entropies ($\Delta S^{\ddagger}$; obtained using site counts measured by H_2O titrations; rates vs H_2O uptakes; Supporting Information section S3). C_3H_8 dehydrogenation rates give an activation barrier of 84 ± 3 kJ mol^{-1}, a value much smaller than previously reported (140 to 300 kJ mol^{-1})[20] for C_3H_8 dehydrogenation on m-ZrO_2 surfaces (8−45 nm crystallites) treated thermally before rate measurements.

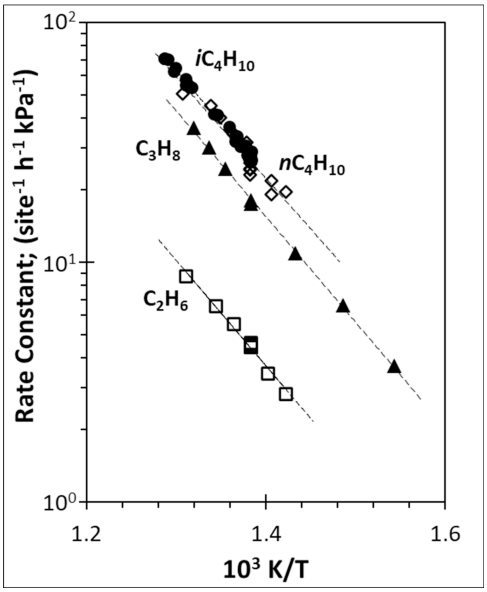

Figure 4. First-order dehydrogenation rate constants (per active site, determined from titration by H_2O during reaction) as a function of temperature in an Arrhenius-type format for C_2H_6 (open squares), C_3H_8 (closed triangles), nC_4H_{10} (open diamonds), and iC_4H_{10} (closed circles) reactants on DME-treated m-ZrO_2. Dashed lines indicate exponential regression.

Dehydrogenation activation barriers for C_2H_6 (84 ± 7 kJ mol^{-1}), nC_4H_{10} (80 ± 18 kJ mol^{-1}), and iC_4H_{10} (83 ± 14 kJ mol^{-1}) alkanes are similar to those for C_3H_8 (84 ± 3). These values reflect barriers for kinetically relevant C−H activation steps, as inferred from kinetic trends for all alkanes (Figure 3) and the normal kinetic isotope effects observed for propane reactants. These barriers and kinetic evidence do not inform us about which C−H bond is activated (or whether the first or the second H-abstraction is involved) in the kinetically relevant step. Their similar values, however, indicate that such a step must involve a C−H bond that is similar in reactivity for each of these alkane reactants. Differences in rate constants among

https://doi.org/10.1021/jacs.4c07766
J. Am. Chem. Soc. 2024, 146, 25710−25726

Table 1. Measured Activation Enthalpies ($\Delta E^{\ddagger}$) and Entropies ($\Delta S^{\ddagger}$) and Reference Gas-Phase Entropies for Light Alkanes at 700 K and 1 bar

			Gas-Phase Entropy at 700 K, 1 bar (J mol^{-1} K^{-1})			
Alkane	Measured $\Delta E^{\ddagger}$ (kJ mol^{-1})	Measured $\Delta S^{\ddagger}$ (J mol^{-1} K^{-1})	Total $S°_{700}$ [a]	Translational $S°_{700,trans}$ [a]	Rotational $S°_{700,rot}$ [a]	Vibrational $S°_{700,vib}$
C_2H_6	84 ± 7	−132 ± 29	290	169	64	57
C_3H_8	84 ± 3	−119 ± 10	360	174	86	100
nC_4H_{10}	80 ± 18	−122 ± 54	410	177	94	139
iC_4H_{10}	83 ± 14	−118 ± 11	430	177	90	163

[a]Standard state entropies determined from NIST;[36] ± represents two standard deviations estimated from linear regression

alkanes appear to reflect predominantly their different $\Delta S^{\ddagger}$ values, which become decreasingly negative (smaller absolute value for entropy loss) for larger alkanes, but within experimental uncertainty [C_2H_6 (−132 ± 29 J mol^{-1} K^{-1}), C_3H_8 (−119 ± 10 J mol^{-1} K^{-1}), nC_4H_{10} (−122 ± 54 J mol^{-1} K^{-1}), and iC_4H_{10} (−118 ± 11 J mol^{-1} K^{-1})].

The heterolytic nature of C−H activation on Zr−O Lewis acid−base pairs[11,12] leads to bound anionic alkyl species and bound cationic hydrogen species (as shown by DFT methods; section 3.6). Bader charge assessments of these species show that they acquire charges of −0.5 and +0.5 e at the relevant TS for the formation of these species; as such, we refer to these species herein as carbanions and protons. Similar barriers for these alkanes suggest that cleavage of the methyl C−H bond (the only common bond type among these alkanes) limits dehydrogenation rates. The reaction energy for heterolytic cleavage of such terminal C−H bonds in gaseous alkanes to form carbanions and protons are, in fact, similar (1751 kJ mol^{-1} for C_2H_6, 1741 kJ mol^{-1} for C_3H_8, and 1726 kJ mol^{-1} for iC_4H_{10}; Table S3). These terminal C−H bonds must also be activated in the first C−H cleavage event, because an initial activation of non-methyl C−H bonds would lead to kinetically relevant H-abstraction from methyl C−H bonds that differs more significantly in electronic character, given the prior adjacent C−H activation, among alkanes (second C−H bond activation energies from methyl groups of gaseous C_2H_6: 681 kJ mol^{-1}; C_3H_8: 752 kJ mol^{-1}; i-C_4H_{10}: 802 kJ mol^{-1}).[36,57]

The heterolytic C−H bond energies at methyl groups in gaseous alkanes to form alkyl carbanions and protons are much larger (1726−1757 kJ mol^{-1}; see the thermochemical cycles in Figure S16)[36,57] than measured activation barriers on m-ZrO_2 for C_2H_6 to C_4H_{10} alkanes (Table 1). These low barriers reflect the stabilization of the fragments formed through their binding at Zr and O surface atoms and their mutual electrostatic attraction as bound species. In the subsequent C−H activation events from alkyl carbanions (formed via proton abstraction from terminal $-CH_3$ groups in alkanes), hydride abstraction enthalpies (to form an alkene by hydride abstraction at C-atoms vicinal to the position of removed proton)[36,57] are much smaller than for the preceding methyl proton abstraction, but vary slightly with alkyl chain length (54 to 65 kJ mol^{-1} from C_2H_6 to iC_4H_{10}) (detailed analysis of thermochemical cycles in Figure S16). These enthalpies are much smaller than for the initial proton abstraction from the terminal $-CH_3$ (1757 to 1726 kJ mol^{-1} from C_2H_6 to iC_4H_{10}).[36,57] The endothermic formation of gaseous carbanions and protons is energetically demanding, but their binding to exposed Zr−O LAB pairs and the prevalent proximity of the bound cationic and anionic fragments provide the requisite stabilization for the TS and the products of the initial proton abstraction that form the bound carbanion and proton. DFT-derived formation energies of bound $nC_3H_7^{\delta-}$-$H^{\delta+}$ pairs from gaseous n-$C_3H_7^-$ and H^+ species on a Zr−O LAB site pair on m-$ZrO_2(\bar{1}11)$ are highly negative (−1709 kJ mol^{-1}), which reflects a strong binding of these species. These findings confirm that the nature of Zr−O sites as a LAB site pair introduces the essential requisites for viable heterolytic routes. In fact, heterolysis on LAB site pairs of ZrO_2 is favored over homolysis, in spite of the more facile nature of the latter process via homogeneous reactions of gaseous alkanes (section 3.4).

3.3. Selectivity to C_3H_8 Dehydrogenation on m-ZrO_2 and Implications on the Dehydrogenation Mechanism.

Homolytic dissociation energies of terminal C−H bonds in gaseous C_3H_8 are 422 kJ mol^{-1} (see reaction energies in Table 2 for homolytic and heterolytic C−H and C−C bond dissociation energies),[36,57] a value much smaller than that for anion-proton formation via its heterolytic counterpart (1741 kJ mol^{-1}),[36,57] but the binding of a gaseous carbanion and proton at Zr−O LAB pairs is much stronger (−1709 kJ mol^{-1}) than for radical-like species on redox-active oxide surfaces that catalyze dehydrogenation via homolytic C−H activation steps (−50 kJ mol^{-1} on MoO_3-based polyoxometalates).[35] Gaseous nC_3H_7 radical fragments cleave methylene C−H bonds to yield C_3H_6 and H_2 (Table 2, bond dissociation energy of 139 kJ mol^{-1}). A competing β-scission reaction to form C_2H_4, CH_3, and H products has a lower dissociation energy (Table 2, 99 kJ mol^{-1}), indicative of a thermodynamic preference for β-scission in homolytic pathways from nC_3H_7 fragments. In contrast, heterolytic activation of C−H bonds in alkanes can form carbanions that subsequently undergo β-hydride elimination to generate C_3H_6 and H_2 with a dissociation energy of 59 kJ mol^{-1} (nC_3H_7) and 47 kJ mol^{-1} (iC_3H_7). These dissociation energies for β-hydride elimination are lower

Table 2. Gas Phase Homolytic and Heterolytic Bond Dissociation Energies for the Terminal (Normal; n) or Central (iso, i) C−H (n, i, n_H, and i_H) in Alkanes and Alkyl Fragments and C−C Cleavage (from Normal and iso C−H Abstraction; n_C and i_C) in Alkyl Fragments[57]

Reaction[a]	Homolytic Dissociation Energy (kJ mol^{-1})	Heterolytic (anion-proton) Dissociation Energy (kJ mol^{-1})
n: $C_3H_8 \rightarrow nC_3H_7 + H$	422	1741
n_H: $nC_3H_7 + H \rightarrow C_3H_6 + 2H$	139	59
n_C: $nC_3H_7 + H \rightarrow C_2H_4 + CH_3 + H$	99	85
i: $C_3H_8 \rightarrow iC_3H_7 + H$	411	1753
i_H: $iC_3H_7 + H \rightarrow C_3H_6 + 2H$	150	47
i_C: $iC_3H_7 + H \rightarrow C_2H_4 + CH_3 + H$	Not reported	72

[a]Nonstoichiometric fragments are depicted as neutral but are either radicals (homolytic) or proton-anion pairs (heterolytic)

https://doi.org/10.1021/jacs.4c07766
J. Am. Chem. Soc. 2024, 146, 25710−25726

than the analogous elimination of a H-radical via homolytic routes, but also smaller than for the competing β-scission reactions in heterolytic routes to form C_2H_4, CH_3^-, and H^+ products. Heterolytic β-scission reaction energies of gaseous species are higher than β-hydride elimination energies (Table 2, 85 vs 59 kJ mol^{-1} and 72 vs 47 kJ mol^{-1} for nC_3H_7 and iC_3H_7, respectively), indicating preference for β-hydride elimination routes in heterolytic pathways and thus high selectivity to alkene products, which contrasts homolytic routes where β-scission reaction energies are lower than a second C−H activation event.

The very high C_3H_6 selectivities in C_3H_8 reactions on m-ZrO_2 are evident from the ratios of dehydrogenation to C−C scission rates shown in Figure 5 (at 793−873 K). The

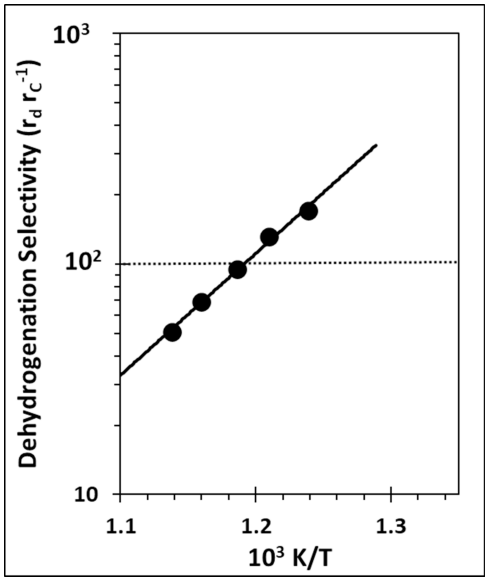

Figure 5. C_3H_8 dehydrogenation selectivity on DME-treated m-ZrO_2. 15 kPa C_3H_8 and 5.1 kPa H_2. Solid lines from exponential regression and horizontal dashed line indicate 99% selectivity.

preference for heterolytic (anion-proton) over homolytic (or cation-hydride heterolysis) C−H activation routes on m-ZrO_2 accounts for such high selectivities (selectivity > 99% for T < 833 K), with trace C−C scission products detected (e.g., CH_4, C_2H_4, and C_2H_6 from C_3H_8). This appears to either reflect β-scission reactions in heterolytic routes that are thermodynamically unfavorable compared to β-hydride elimination, as suggested by bond dissociation energies (Table 2) or a relatively facile C−C bond activation in alkenes.[57]

The higher selectivities observed at lower temperatures reflect apparent C−C cleavage barriers that are about 100 kJ mol^{-1} larger than those for β-hydride elimination in bound propyl carbanions. These differences are directionally similar to thermochemical estimates of heterolytic reaction energies (139 vs 59 kJ mol^{-1} for C−C and C−H activation in gaseous nC_3H_7 carbanions, respectively; Table 2) and with DFT-based assessments of C−X activation barriers from bound nC_3H_7 carbanions at which Zr−O pair in m-ZrO_2(111) surfaces (barriers of 102 kJ mol^{-1} for β-hydride elimination, X = H; 213 kJ mol^{-1} for C−C cleavage, X = C). These DFT-derived differences in barriers (80 kJ mol^{-1} by reaction energy estimates; 111 kJ mol^{-1} by DFT-assessed barriers) are similar to those measured from the data in Figure 6 for C_3H_8 reactants. These observations confirm the heterolytic nature

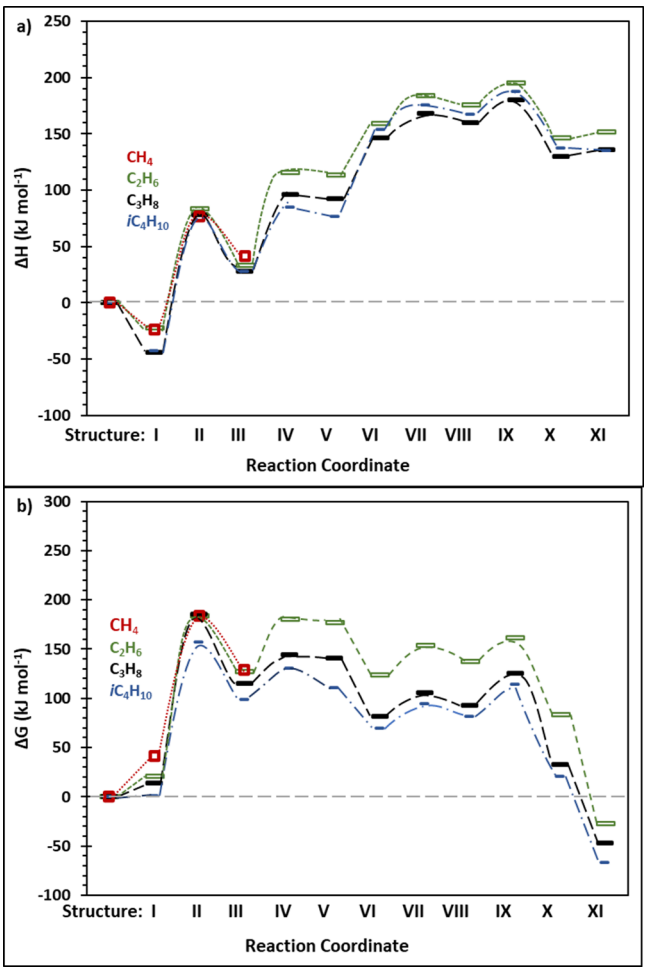

Figure 6. Reaction coordinate diagram showing the change in enthalpy (top) and free energy (bottom) for CH_4 (red open squares, dotted line), C_2H_6 (green open rectangles, short dashed line), C_3H_8 (black large closed rectangles, long dashed line), and iC_4H_{10} (blue small closed rectangles, dashed and dotted line), dehydrogenation referenced to bare m-$ZrO_2(\bar{1}11)$ surface and gaseous alkane at 1 and 723 K and dehydrogenating to 0.001 bar of alkene and 0.01 bar of H_2. Reaction enthalpies can be computed by comparing the initial bare surface and gaseous alkane enthalpy to the product H_2, alkene, and bare surface enthalpy (XI) for each C_2H_6 (152 kJ mol^{-1}), C_3H_8 (136 kJ mol^{-1}), and iC_4H_{10} (137 kJ mol^{-1}); these values are comparable to those tabulated from thermodynamic data (142, 129, and 123 kJ mol^{-1}, respectively).

of C-X activation at Zr−O pairs on stoichiometric ZrO_2 surfaces. They contradict the expectations from homolytic activation routes at O-vacancies, proposed to form by treatments in CO at 823 K, which lead to modest rate enhancements compared with m-ZrO_2 surfaces treated with DME to react with surface titrants.[41,47] The same general trends are evident for other alkanes (e.g., nC_4H_{10}, see Figure S10); reactions with nC_4H_{10} also exhibit increasing dehydrogenation selectivity at lower temperatures, but with a cracking barrier estimated at only 40 kJ mol^{-1} higher than for dehydrogenation. The smaller difference in β-scission and β-hydride elimination is expected from gas phase thermodynamics of nC_3H_7 and iC_4H_9 anionic fragments, where the difference in the two competing pathway reaction energies for each species are −26 and −22 kJ mol^{-1}, respectively.

https://doi.org/10.1021/jacs.4c07766
J. Am. Chem. Soc. 2024, 146, 25710−25726

C−H bond heterolysis and the anionic nature of the alkyl fragments bound at Zr−O LAB pairs lead to relative rates of β-hydride abstraction and β-scission of C−C bonds that differ markedly from those in homolytic routes that form radical-like alkyls and heterolytic routes that form alkyl carbenium ions. As a result, reactions of C_3H_8 on m-ZrO_2 selectively form C_3H_6 over CH_4/C_2H_4 (Figure 5). Such preferences are also evident from the reaction energies for cleaving C−H and C−C bonds in C_3H_8 when comparing homolytic and heterolytic cleavage in gaseous molecules (Table 2).

3.4. Effect of Alkane Chain Size on Dehydrogenation Rates on DME-Treated m-ZrO_2 Surfaces. Measured C_3H_8 dehydrogenation activation barriers on DME-treated m-ZrO_2 (84 ± 3 kJ mol^{-1}) are much smaller than reported previously on m-ZrO_2 catalysts treated thermally (N_2, 823 K; from 140 to 300 kJ mol^{-1} for ZrO_2 crystallites 8−45 nm in diameter).[47] Chemical reagents (other than DME) are also effective at reacting with bound H_2O or CO_2 to uncover the most competent Zr−O site pairs and also lead to low activation barriers.[18,19] These reagents include the alkene products formed in dehydrogenation reactions; as in the case of DME, they can remove bound H_2O (and CO_2) via their hydrolysis and reforming reactions. Consequently, titrants can be removed during dehydrogenation to an extent that depends on the temperature, impurity levels (O_2 and/or its H_2O and CO_2 products), and prevalent concentrations and identity/reactivity of the product alkenes. The higher apparent barriers measured on thermally treated ZrO_2 from temperature increase protocols are likely partially derived from the uncovering of active sites as temperature and alkane conversion levels increase (together with a greater extent of impurity thermal desorption) instead of the inherent kinetic barriers for C−H activation steps. The uncovering of such surface sites at higher temperatures leads to cleaner surfaces, which remain uncovered as temperatures are subsequently decreased; such effects are evident from measured barriers that are about 90 kJ mol^{-1} higher during temperature increase (200 ± 6 kJ mol^{-1}, Figure S7) than subsequent temperature decrease (110 kJ mol^{-1}, Figure S7) protocols. These values are similar to those measured on DME-treated samples with increasing temperature (84 ± 3 kJ mol^{-1}, Figure 4), on which such active sites were already uncovered at low temperatures by chemical treatment and higher temperatures where product-induced titrant desorption processes become inconsequential.

The ability of alkenes to scavenge titrants during alkane dehydrogenation may lead to a different number of uncovered active sites, depending on the identity and concentration of such products during reactions of each alkane. In such cases, measured activation barriers may reflect the combined effects of temperature and conversion on intrinsic kinetic trends as well as the effectiveness of each alkene product in scavenging bound titrants, thus interfering with direct assessments of the chemical origins of reactivity and activation barriers for each alkane. Such interference can be circumvented by using alkane mixtures, for which each alkane reacts on surfaces exposed to the same mixture of alkene products. The ratio of the dehydrogenation rate constants for a mixture of C_3H_8 and C_2H_6 reactants was measured at 700−873 K upon an increase and then decrease in temperature (shown in Figure S11). The ratio was 4−5 throughout this wide range of temperatures and was similar to those essentially constant ratios (4.1 ± 0.1) throughout this temperature range when C_3H_8 and C_2H_6 dehydrogenation rates were measured independently (Figure 4, dashed line in Figure 6). As such, the most substantial contributions to the differences in rate among alkanes in this temperature range arise from factors outside of enthalpic barriers.

The similar activation barriers for C_2-C_4 alkanes indicates that their different rate constants (Figure 4) predominantly reflect differences in their pre-exponential factors and thus in their respective activation entropies ($\Delta S^{\ddagger}$); these differences reflect, in turn, the entropy changes involved in forming the kinetically relevant C−H activation TS from a gaseous alkane and a bare surface. These activation entropies are shown in Table 1 for each alkane and were obtained from their respective rate constants (per site) by:

$$k_{C-H} = \frac{\kappa k_B T}{h} e^{-\Delta S^{\ddagger}/R} e^{-\Delta H^{\ddagger}/RT} \quad (4)$$

These $\Delta S^{\ddagger}$ values become more negative with decreasing alkane size, but remain similar for the different alkanes within experimental uncertainty [C_2H_6 (-132 ± 29 J mol^{-1} K^{-1}), C_3H_8 (-119 ± 10 J mol^{-1} K^{-1}), $n$$C_4H_{10}$ (-122 ± 54 J mol^{-1} K^{-1}), and $i$$C_4H_{10}$ (-118 ± 11 J mol^{-1} K^{-1}), a difference of 14 J mol^{-1} K^{-1} among alkanes]. This trend is anticipated from the relative magnitude of the rate constants for each alkane (Figure 4).

ΔS values can be dissected into their vibrational (ΔS_{vib}), translational (ΔS_{trans}), and rotational (ΔS_{rot}) contributions for the kinetically relevant TS relative to the gaseous alkane and a bare LAB site. The vibrational component of entropy for gaseous alkanes ($S°_{vib}$, Table 1)[37] shows the largest differences among alkanes (from 57 to 163 J mol^{-1} K^{-1} from C_2H_6 to $i$$C_4H_{10}$, 723 K; Table 1); however, the change in vibrational modes upon C−H abstraction at the TS, a bond which accounts for ∼ 8 J mol^{-1} K^{-1} of the S_{vib}, is anticipated to be nearly identical for each alkane and not meaningfully contribute to the observed differences in rate constant prefactors among alkanes. Translational entropies ($S°_{trans}$) and rotational entropies ($S°_{rot}$) derived from statistical mechanics formalisms[37] (see Supporting Information section S7) are similar among these alkanes (Table 2, translational: 169 to 177 J mol^{-1} K^{-1} and rotational: 64 to 90 J mol^{-1} K^{-1} for C_2H_6 to $i$$C_4H_{10}$;). The weak binding at the TS is likely to cause a loss of translational freedom, with a loss of $0.3S_{trans,gas}$ + $0.3S_{rot,gas}$ derived from trends in binding energy for species that bind strongly and lead to high coverages on catalytic sites, which contrasts the molecular adsorption of alkane-derived species on m-ZrO_2.[58] Given the differences in S_{trans} and S_{rot} values among alkanes, this treatment would only account for 10 J mol^{-1} K^{-1} of the measured differences in $\Delta S^{\ddagger}$ among alkanes. Since these combined effects do not account for the measured 15 J mol^{-1} K^{-1} differences in $\Delta S^{\ddagger}$ among alkanes, heterolytic dehydrogenation of weakly bound alkanes (ΔH = −24 to −44 kJ mol^{-1}, decreasing with alkane size; section 3.5) on LAB site pairs of ZrO_2 apparently depart such conventions for adsorbed species entropy.

The binding of TS structures at surfaces inhibits translational and rotational freedom to an extent that depends on the binding strength and structural arrangement of the reacting moiety with the surface. Alkane C−C activation reactions were previously shown to exhibit relative rate constants among alkanes of contrasting chain length, driven predominantly by the entropy of the bound alkyl fragment,[59] where long-chain n-alkanes retained a much larger fraction of their entropy upon adsorption, resulting in larger turnover rates for increasing

https://doi.org/10.1021/jacs.4c07766
J. Am. Chem. Soc. 2024, 146, 25710−25726

alkane chain length. This results from fragments of the adsorbed alkanes retaining mobility in the form of residual rotational, translational, and configurational entropy due to the ends of the molecules being bound to the surface and the rest of the molecule being relatively unconstrained. For C−C activation, two C-atoms formed bonds to the surface, limiting the pendent groups to 1D rotational motion. In the case of C−H activation in this work, only one C-atom is constrained to the surface (section 3.5), enabling a greater degree of molecular mobility and thus accounting for the observed trends in dehydrogenation rate constants with alkane chain length.

3.5. DFT-Based Mechanistic Assessments of Alkane Dehydrogenation Rates on Lewis Acid−Base Pairs at *m*-$ZrO_2(\bar{1}11)$ Surfaces. DFT-derived energies along the dehydrogenation reaction coordinate for each alkane are used here to do the following:

i assess the identity, reversibility, and kinetic relevance of elementary steps in the dehydrogenation reaction sequence
ii confirm the heterolytic character and the location of each of the two required C−H activation steps
iii demonstrate the weak binding of all species and the uncovered nature of catalytically competent Zr−O pairs during catalysis

These objectives are addressed first for C_2H_6 dehydrogenation on the Zr−O pairs that bind H_2O most strongly (electronic water adsorption energy of −132 kJ mol^{-1} where values range up to −21 kJ mol^{-1} for different Zr−O pairs) at *m*-$ZrO_2(\bar{1}11)$ surfaces. This Zr-atom (Zr_{II} site in Figure 1) is bound to the two-coordinate O-atom along the + *a*-axis (Figure 1) and is used as the model Zr−O LAB site pair to assess plausible pathways for the C_3H_8 dehydrogenation routes.

The catalytic cycle developed here from DFT-derived energies and the bound intermediates and transition states involved is depicted in Scheme 1 and resembles dehydrogenation mechanisms described by Tanabe et al. for the dehydrogenation of oxygenates.[13,14] The requisite steps involve

Scheme 1. Catalytic Cycle for C_nH_{2n+2} Dehydrogenation on ZrO_2[a]

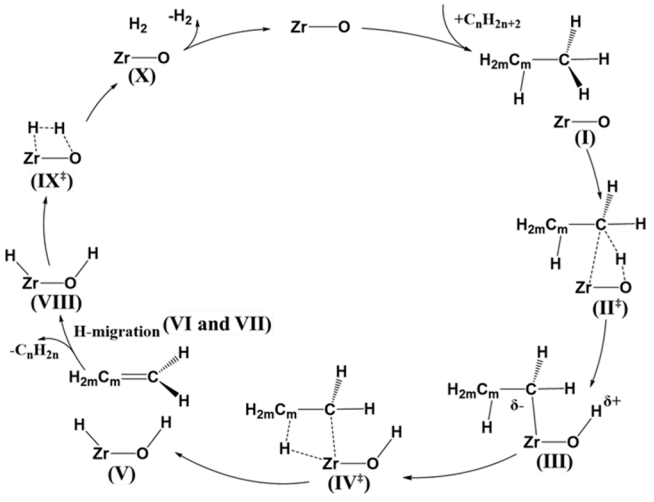

[a]Roman numerals correspond to the structures of intermediates and TS. *n* is the carbon number of the alkane, used in the scheme to account for a range of alkanes; *m* is (*n* − 1).

C_nH_{2n+2} binding (n is the number of carbon atoms in the alkane) to form an undissociated bound alkane (species I), heterolytic cleavage of a terminal C−H bond (mediated by the TS depicted as species $II^{‡}$) to form bound protons and alkyl carbanions (species III), *β*-H-elimination via TS depicted as species $IV^{‡}$ to form gaseous C_nH_{2n} and H^--H^+ pairs bound at Zr−O site pairs (V), desorption of C_nH_{2n} (species VI), migration of H^- (species VII) to form a closely coordinated H^--$H,^+$ (species VIII), the reaction of H^- and H^+ (species IX) to form H_2 (species X), and its subsequent desorption to recover the bare Zr−O site pair (XI).

The reaction coordinate diagrams in Figure 6 show the enthalpy (top) and free energy (bottom) (electronic energies, enthalpies, and free energies also shown in Table 3; calculation methods are described in section 2.3) for each elementary step and intermediate in the dehydrogenation of C_2H_6, C_3H_8, and iC_4H_{10} alkanes and for the adsorption and first C−H abstraction step from CH_4 (note that subsequent steps involve the formation of gaseous methylene species, a step that is energetically infeasible). The kinetic relevance of a given step is dictated by the relative heights of the free energy barriers; those barriers that are higher are more kinetically relevant, making reaction coordinate diagrams a visual tool in such assessments.

Computation of these free energies requires entropies for each step gaseous species and their surface bound analogs. Due to the failure of harmonic oscillators in describing low frequency modes in vibrational assessments, estimations of surface entropies are frequently derived from gaseous analogs (section 2.3). The entropies of gaseous species, and thus their bound analogs, depend on the prevalent pressure of the gas, where deviations from a standard state of 1 bar arise directly from the translational entropy and the gaseous entropy gain compared to $S_{trans,1bar}$ is $R{\cdot}\ln(P{\cdot}P^{-1}{}_{1bar})$. Due to these strong pressure effects in entropy, the prevalent pressure of products and reactants impacts the free energy along the reaction coordinate. This is most evident by observing the free energy of reaction at standard conditions of 1 bar (the final state (XI) in the reaction coordinate diagram depicted in Figure S13 for standard free energies), where free energies of reaction are positive, indicative of a preference for hydrogenation in spite of experimental measurements of dehydrogenation. This contrast arises from the gaseous pressures in the reactor, which are not the typical standard state pressures (1 bar of alkane, alkene, and H_2 each at 723 K) where hydrogenation is thermodynamically favored. Selection of gaseous species pressures commensurate with those of reactants and products in the reactor (i.e., 1 bar alkane, 0.01 bar H_2, and 0.001 bar alkene) enables analysis of the free energy of alkane dehydrogenation reactions for conditions relevant to catalysis. This free energy profile, shown in Figure 6b, depicts negative free energies of reaction under these conditions, which is consistent with experimental assessments.

The lower product pressure in the reactor not only provides the favorable thermodynamics that enable dehydrogenation, but also results in entropy gains for product-like TS and intermediates and desorption steps in comparison to the standard condition of 1 bar (see Figure S13 for reaction coordinate diagrams at 1 bar of all species). This entropy gain manifests as lower free energies in the later steps of the reaction coordinate where products have been formed and when they desorb, making the pathway increasingly favorable as product pressures decrease. This section more thoroughly

https://doi.org/10.1021/jacs.4c07766
J. Am. Chem. Soc. 2024, 146, 25710−25726

Table 3. DFT Energies of C_2H_6, C_3H_8, and iC_4H_{10} Dehydrogenation on m-$ZrO_2(\bar{1}11)$[a]

Structure	Description	ΔE (kJ mol^{-1})	ΔH (kJ mol^{-1})	ΔS (J mol^{-1} K^{-1})	ΔG (kJ mol^{-1})
0	$ZrO_{2,bare}$	0	0	0	0
I_{C1}	$ZrO_{2,CH4*}$	−18	−24	−96	45
$II^{‡}_{C1}$	$(ZrO_{2,CH3*-H*})^{‡}$	88	77	−162	194
III_{C1}	$ZrO_{2,CH3*-H*}$	+40	+42	−133	+138
0	$ZrO_{2,bare}$	0	0	0	0
I_{C2}	$ZrO_{2,C2H6*}$	−28	−22	−59	+21
$II^{‡}_{C2}$	$(ZrO_{2,C2H5*-H*})^{‡}$	88	84	−138	184
III_{C2}	$ZrO_{2,C2H5*-H*}$	+32	+33	−129	+127
$IV^{‡}_{C2}$	$(ZrO_{2,C2H4*-2H*})^{‡}$	131	116	−89	180
V_{C2}	$ZrO_{2,C2H4*-2H*}$	+127	+114	−88	+177
VI_{C2}	$ZrO_{2,C2H4-2H*}$	+168	+159	49	+124
$VII^{‡}_{C2}$	$(ZrO_{2,C2H4-2H**})^{‡}$	198	184	42	153
$VIII_{C2}$	$ZrO_{2,C2H4-2H**}$	+183	+175	52	+137
$IX^{‡}_{C2}$	$(ZrO_{2,C2H4-H2*})^{‡}$	221	195	46	162
X_{C2}	$ZrO_{2,C2H4-H2*}$	+157	+146	87	+83
XI_{C2}	$ZrO_{2,C2H4-H2}$	+171	+152	247	−27
0	$ZrO_{2,bare}$	0	0	0	0
I_{C3}	$ZrO_{2,C3H8*}$	−36	−44	−80	14
$II^{‡}_{C3}$	$(ZrO_{2,C3H7*-H*})^{‡}$	90	78	−149	185
III_{C3}	$ZrO_{2,C3H7*-H*}$	+28	+27	−121	+115
$IV^{‡}_{C3}$	$(ZrO_{2,C3H6*-2H*})^{‡}$	107	96	−66	144
V_{C3}	$ZrO_{2,C3H6*-2H*}$	+102	+92	−68	+141
VI_{C3}	$ZrO_{2,C3H6-2H*}$	+156	+147	90	+81
$VII^{‡}_{C3}$	$(ZrO_{2,C3H6-2H**})^{‡}$	184	168	87	105
$VIII_{C3}$	$ZrO_{2,C3H6-2H**}$	+168	+160	92	+93
$IX^{‡}_{C3}$	$(ZrO_{2,C3H6-H2*})^{‡}$	204	180	76	125
X_{C3}	$ZrO_{2,C3H6-H2*}$	+145	+130	135	+32
XI_{C3}	$ZrO_{2,C3H6-H2}$	+156	+136	254	−47
0	$ZrO_{2,bare}$	0	0	0	0
I_{C4}	$ZrO_{2,C4H10*}$	−40	−43	−60	1
$II^{‡}_{C4}$	$(ZrO_{2,C4H9*-H*})^{‡}$	82	73	−116	157
III_{C4}	$ZrO_{2,C4H9*-H*}$	+23	+28	−98	+99
$IV^{‡}_{C4}$	$(ZrO_{2,C4H8*-2H*})^{‡}$	96	85	−63	130
V_{C4}	$ZrO_{2,C4H8*-2H*}$	+81	+77	−47	+110
VI_{C4}	$ZrO_{2,C4H8-2H*}$	+145	+154	116	+70
$VII^{‡}_{C4}$	$(ZrO_{2,C4H8-2H**})^{‡}$	176	175	112	94
$VIII_{C4}$	$ZrO_{2,C4H8-2H**}$	+160	+167	118	+82
$IX^{‡}_{C4}$	$(ZrO_{2,C4H8-H2*})^{‡}$	199	187	102	114
X_{C4}	$ZrO_{2,C4H8-H2*}$	+135	+137	161	+21
XI_{C4}	$ZrO_{2,C4H8-H2}$	+149	+135	279	−67

[a]At 723 K for 1 bar reactants and 0.01 bar H_2 and 0.001 bar alkene of products.

analyzes this reaction coordinate diagram (Figure 6) and discusses it in the context of standard state free energies (Figure S13).

The alkane dehydrogenation process is depicted in Scheme 1 and energies for each species along the reaction coordinate are listed in Table 3. The corresponding reaction coordinate diagram is shown in Figure 6 and DFT-derived structures for which energies are reported are depicted in Figure 7. C_2H_6 reactions involve the weak binding of undissociated reactants at Zr−O site pairs (ΔH = −22 kJ mol^{-1}, ΔG_{723K} = + 21 kJ mol^{-1}, structure I_{C2}, where subscript Cn refers to the step for the alkane with carbon number n, C_nH_{2n+2}). In structure I_{C2}, one of the two CH_3 groups interacts weakly with the O-atom (Figure 7), while the other CH_3 group in C_2H_6 shows no evidence of interactions with the surface and is directed away from the surface, consistent with weak binding and with the low reactant coverages and essentially bare surfaces evidenced by dehydrogenation rates that depend linearly on alkane pressures for all reactants. C−H activation can occur at one of the two terminal C-atoms to form either a hydride and alkyl carbenium ion or a proton and an alkyl carbanion, with the corresponding anionic and cationic fragments interacting with the Zr and O centers, respectively. Our DFT computations show that that proton abstraction is favored over hydride abstraction routes in the first C−H activation step for C_3H_8 ($\Delta E^{‡}$: 90 vs 213 kJ mol^{-1}). Proton abstraction from C_2H_6 occurs from structure I_{C2} via the TS $II_{C2}{}^{‡}$ structure to form an ethyl carbanion bound at the Zr center and a proton at the vicinal O-atom (III_{C2}), as expected from heterolytic cleavage. H_2 dissociation has been shown to occur heterolytically on ZrO_2 sites by infrared spectroscopy (m-ZrO_2 and t-ZrO_2),[60] exchange reactions (m-ZrO_2),[13] and theory (ZrO_2 clusters).[61] The Zr−O bond lengthens (from 2.005 to 2.258 Å) as the C−H bond is cleaved in this step. The free energy of formation of structure $II_{C2}{}^{‡}$ from gaseous C_2H_6 and a bare site is 184 kJ mol^{-1} and the corresponding formation enthalpy is 84 kJ

https://doi.org/10.1021/jacs.4c07766
J. Am. Chem. Soc. 2024, 146, 25710−25726

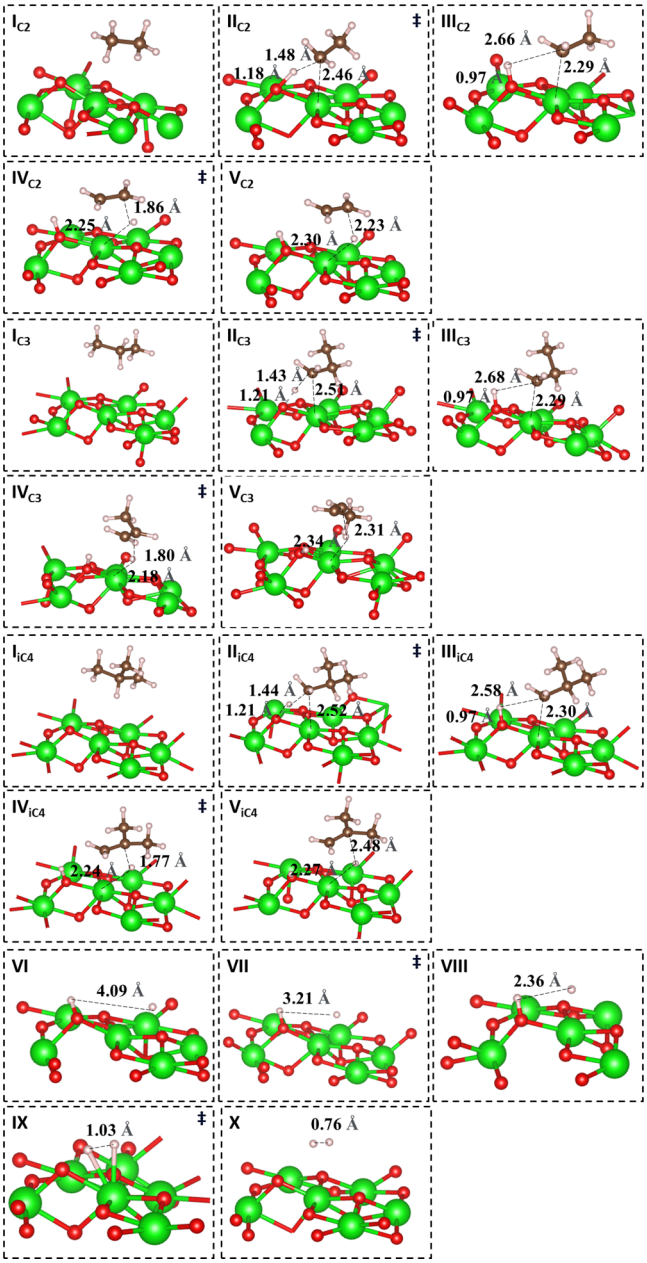

Figure 7. Ball and stick representations of structures from the reaction coordinate diagram showing the reaction of alkanes C_2H_6 (C2), C_3H_8 (C3), and iC_4H_{10} (iC4) in dehydrogenation on *m*-$ZrO_2(\bar{1}11)$. Zr: green; O: red; H: white; C: brown. Note that the models for structures VI and higher are the same for all alkanes since they involve common H-migration and reactions steps, but the energies (Table 3) differ due to contrasting alkene species.

mol^{-1}. The bound C_2H_5 carbanion-proton pair has an enthalpy of formation of + 33 kJ mol^{-1} and a free energy of formation of + 127 kJ mol^{-1} from a bare Zr−O surface pair and a gaseous C_2H_6 molecule. These proton and anion products of C−H activation events are stabilized via electrostatic interactions with each other and with the LAB site pair, enabling their formation during heterolysis. As such, alternative mechanisms involving the migration of these cation−anion pairs to other Zr and O sites necessitate that they migrate in concert to a different site but remain within interacting distances to benefit from the electrostatic stabilization. Such migration would involve moving the cation−anion pair to Zr−O pairs, where they would be less stable than on the most competent C−H activation sites at which they formed. The strict requirement of comigration to a weaker-binding site limits the viability of a site migration-involved mechanisms."

The second C−H activation step involves *β*-hydride abstraction from the intact CH_3 in the C_2H_5 carbanion (III_{C2}) via TS $IV_{C2}^{‡}$ structures that form a product state, species V_{C2}, comprised of a weakly bound alkene and a proton-hydride pair on the surface. The structure of TS $IV_{C2}^{‡}$ resembles that of species V_{C2}, which is indicative of a very late TS for the *β*-hydride elimination elementary step. Specifically, the two structures exhibit comparable Zr−O bond lengths (2.274 and 2.272 Å for $IV_{C2}^{‡}$ and V_{C2}, respectively), and the alkene product has been nearly formed at this late TS (C−C bond length of 1.37 vs 1.35 Å, respectively). The free energy of formation of this transition state from gaseous alkane and a bare Zr−O pair is 180 kJ mol^{-1} and its formation enthalpy is 116 kJ mol^{-1}, which is similar to those of product state species V_{C2} (ΔG = +177 kJ mol^{-1}, ΔH = +114 kJ mol^{-1}, Table 3). The abstracted hydride resides in a hollow between Zr_I and Zr_{II} atoms (Figure 1).

The species formed by C_2H_4 desorption (species VI_{C2}) gains entropy (ΔS: 49 J mol^{-1} K^{-1}) by forming a freely translating and rotating gaseous species, leading to a decrease in free energy from its precursor species V_{C2} (ΔH = +159 kJ mol^{-1}, ΔG_{723K} = +124 kJ mol^{-1}, Table 3). The elementary step involves the migration of the H^- formed to the atop position of the Zr_{II} atom bound to the O-atom that stabilizes the proton ($VII_{C2}^{‡}$, $\Delta H^{‡}$ = 184 kJ mol^{-1}, $\Delta G^{‡}$ = 153 kJ mol^{-1}) to form a vicinal proton-hydride pair ($VIII_{C2}$, ΔH = +175 kJ mol^{-1}, ΔG = +137 kJ mol^{-1}, Table 3). This pair combines ($IX_{C2}^{‡}$, $\Delta H^{‡}$ = 195 kJ mol^{-1}, $\Delta G^{‡}$ = 162 kJ mol^{-1}) to form a bound H_2 molecule (X_{C2}, ΔH = +146 kJ mol^{-1}, ΔG = +83 kJ mol^{-1}) that desorbs, thus restoring the bare Zr−O pair and completing a catalytic turnover (species XI_{C2}, ΔH = +152 kJ mol^{-1}, ΔG = −27 kJ mol^{-1}).

The first C−H abstraction in C_2H_6 (from either CH_3 group) forms a surface proton and a bound carbanion with an enthalpy barrier (84 kJ mol^{-1}) that is similar to that experimentally observed (shown for ethane as 84 ± 7 kJ mol^{-1}). The second C−H abstraction TS ($IV^{‡}_{C2}$) exhibits a slightly higher barrier in enthalpy (116 kJ mol^{-1}), than that of the first C−H cleavage (for C_2H_6, Table 3), but a slightly lower free energy barrier (180 kJ mol^{-1}). The reaction coordinate diagram in Figure 6 shows enthalpy barriers for H_2 migration and combination that are larger than for both C−H activation barriers and measured ones, a finding that seems inconsistent with the kinetic relevance of the C−H activation steps. This is a consequence of endothermic reactions whose energy must increase to that of products along the reaction coordinate; enthalpy barriers obtained by visual inspection of the reaction coordinate diagram could never be smaller than the overall reaction energy in spite of the low measured barriers. The kinetic relevance of a step is determined, however, by the relative activation free energies among all steps along a reaction coordinate, not the enthalpy of a given TS. Accordingly, measured activation barriers from Arrhenius treatments of rate data reflect the enthalpy barrier for the step with the highest free energy along the overall reaction coordinate. Visual inspection of the free energy diagram (Figure 7) indeed shows that H_2 recombination and desorption show lower free energy barriers than those for C−H activation steps because of the significant entropy gains upon desorption. Given this

https://doi.org/10.1021/jacs.4c07766
J. Am. Chem. Soc. 2024, 146, 25710−25726

inspection, it is the first C−H activation that is kinetically relevant for C_2H_6 reactants, but the second C−H activation barrier is similar. Analysis of C−H activation for other alkanes provides further insights into the free energy landscape of the reaction coordinates in alkane dehydrogenation.

Enthalpies and free energies were also examined for CH_4 (up to the formation of the methyl carbanion), C_3H_8, and iC_4H_{10} dehydrogenation catalytic sequences. Figure 6 shows DFT-derived enthalpies and free energies for CH_4, C_2H_6, C_3H_8, and iC_4H_{10} dehydrogenation at the Zr_{II}-O site pair on m-$ZrO_2(\bar{1}11)$. The relevant structures of the bound species involved in the C_3H_8 and i-C_4H_{10} reactions are depicted in Figure 7. These C−H, O−H, C−Zr, and H−Zr bond lengths are similar at each step among alkanes, suggesting that they can react on Zr−O site pairs through similar pathways. In contrast with C_2H_6, C_3H_8 and iC_3H_{10} molecules have nonterminal C−H bonds that must be activated at some stage along the reaction coordinate in completing a dehydrogenation turnover. Proton abstraction from terminal $-CH_3$ groups occurs with a slightly lower free energy barrier (186 vs 190 kJ mol^{-1}) than from parallel pathways from methylene $-CH_2-$ groups in C_3H_8 dehydrogenation on the m-$ZrO_2(\bar{1}11)$ surface. The enthalpy of formation of the TS for proton abstraction at the CH_2 group in C_3H_8 is 86 kJ mol^{-1}, a value similar to that for abstraction from the CH_3 group (78 kJ mol^{-1}). The enthalpy of formation for the C−H activation TS for CH_4 is similar to that for C_2H_6 and C_3H_8 at 77 kJ mol^{-1}; these observations indicate that the barrier for proton abstraction is essentially insensitive to the type of C−H bond cleaved in forming a proton and an alkyl carbanion at Zr−O site pairs. Also, the enthalpy barrier to form the β-hydride elimination TS in a subsequent step is lower by 24 kJ mol^{-1} from the nC_3H_7 anion formed via terminal proton abstraction than that from iC_3H_7 carbanions, indicative of a preference for dehydrogenation sequences that proceed via nC_3H_7 intermediates.

The reaction enthalpy to bind alkanes on ZrO_2 surfaces is more negative for larger alkanes (−24 kJ mol^{-1} for CH_4; −25 kJ mol^{-1} for C_2H_6; −44 kJ mol^{-1} for C_3H_8; −43 kJ mol^{-1} for iC_4H_{10}); these differences predominantly reflect van der Waals interactions that are also responsible for their condensation as liquids. The concomitant loss of entropy upon adsorption leads, however, to positive adsorption free energies for all alkanes, consistent with the low coverages prevalent during steady-state catalysis at 700−900 K). The subsequent abstraction of a proton at the methyl C-atom (C^a) in these alkanes involves a similar TS structure ($II^{\ddagger}_{nC}$, Figure 7 and Table 3) for these alkanes $[n\text{-}C_xH_{2x+1}\cdots Zr-O\cdots H]^{\dagger}$. The enthalpies of formation of this C−H cleavage TS from the gaseous alkane and bare surface in structure $II^{\ddagger}$ are similar among alkanes (84, 84, 78, and 76 kJ mol^{-1}, with increasing alkane size from CH_4 to iC_4H_{10}) consistent with the similar values of their experimentally measured activation barriers (Figure 4).

The formation enthalpies of the bound carbanion formed in Species III [n-C_xH_{2x+1}-Zr···O-H, III_{nC}] decreased slightly from + 33 kJ mol^{-1} to + 27 kJ mol^{-1} with increasing size (C_2H_6 to i-C_4H_{10}). Deprotonation typically becomes less endothermic with alkane size for their gaseous counterparts (+1757, +1741, and +1726 kJ mol^{-1} for C_2H_4, C_3H_8, and iC_4H_{10}[36]). Born−Haber thermochemical cycles (Figure S15) demonstrate that the large differences between heterolytic dissociation energies of an alkane (or H_2, H_2O) into gaseous or bound ions reflects the strong stabilization of the proton-carbanion by ZrO_2 and by electrostatic interactions between the two fragments enabled by their vicinal locations at the Zr and O atoms.[62]

β-Hydride elimination from the $[n\text{-}C_xH_{2x+1}\text{-}Zr\cdots O\text{-}H](a)$ carbanion is mediated by TS structure $IV^{\ddagger}_{nC}$, which forms a weakly adsorbed alkene and a bound proton-hydride pair, $C_xH_{2x}\cdots H\text{-}Zr\text{-}O\text{-}H(a)$ ($\Delta H^{\ddagger}$ = 96 kJ mol^{-1}, $\Delta G^{\ddagger}$ = 144 kJ mol^{-1} for C_3H_8 and $\Delta H^{\ddagger}$ = 85 kJ mol^{-1}, $\Delta G^{\ddagger}$ = 130 kJ mol^{-1} for iC_4H_{10}). These TS transition state structures for β-hydride elimination of each alkyl-carbanion $[n\text{-}C_xH_{2x}\cdots H\text{-}Zr\cdots O\text{-}H]^{\dagger}(a)$ resemble their respective product states (bound alkenes and hydride proton pair (V_{nC}), ΔH = +92 kJ mol^{-1} for C_3H_8 and ΔH = +77 kJ mol^{-1} for iC_4H_{10}, Figure 7), as also shown for C_2H_6 reactants. The consequent late character of this β-hydride elimination TS (Figure 7, Table 3) is also evident from its structural resemblance to its product state. The formation free energy of this $[n\text{-}C_xH_{2x+1}\cdots H\text{-}Zr\cdots O\text{-}H]^{\dagger}(a)$ TS from a gaseous alkane and a bare site decreases with increasing alkane size C_2H_6 to iC_4H_{10} (180, 144, and 130 kJ mol^{-1}, respectively; Figure 7, Table 3). The hydride in Structure VI bridges Zr_I and Zr_{II} atoms, as also observed for C_2H_6 (Figure 7) and the subsequent step comprising H_2 formation and desorption are analogous to that of C_2H_6 dehydrogenation (Figure 7).

Activation enthalpies for the DFT-derived first C−H abstraction TS (84 kJ mol^{-1}) are similar among alkanes and consistent with experiments (84 ± 3 kJ mol^{-1}); however, it is free energy barriers that dictate the kinetic-relevance of steps. These DFT-derived formation free energies for C−H abstraction TS suggest that the first proton abstraction from terminal $-CH_3$ groups is the predominant kinetically relevant step for C_2H_6, C_3H_8, and i-C_4H_{10} dehydrogenation reactions, based on the magnitude of the barrier for each C−H abstraction step alone. Though the kinetically relevant step determined by free energies at reaction conditions (Figure 7) is clear, it is noted that those determined by standard state free energies are not as definitive for one of the studied alkanes, with the free energy barriers (at 1 bar, Figure S13) of the first C−H activation in C_2H_6 dehydrogenation being lower than that determined from the second C−H activation (184 vs 213 kJ mol^{-1}, respectively). This apparent disparate finding may be explained by the assumptions made in computing the ΔS values, namely, i) the relevant pressure of product and reactant molecules, ii) the method selected to circumvent DFT inadequacies in assessing entropy contributions from low-frequency modes of bound intermediates and transition states, and iii) the use of Zr−O structural models that do not account for the requisite coordinative unsaturation inferred from trends in areal site densities (discussed in section 3.6)

The prevailing pressure of gaseous species (potential source i) is a factor that determines the entropy of gaseous molecules (see eq S10 and discussion above). Comparison of free energies at relevant gas phase pressures (Figure 7 and Figure S14 at 873 K) and 1 bar (Figure S13) shows that the kinetic relevance of steps can depend, in part, on the conditions of the reaction (T, P, etc.) and which side of thermodynamic equilibrium the gas phase resides. This results from product pressures that, when low as during the reported catalytic assessments, decrease the free energy for product-like intermediates and TS (i.e., β-hydride abstraction in TS $IV^{\ddagger}$). Such relevant pressures were assumed to be similar for all alkanes (Figure 7), but C_2H_6 dehydrogenation necessarily had lower C_2H_4 pressures by virtue of lower rates under similar reactor conditions and more strict thermodynamic constraints.

https://doi.org/10.1021/jacs.4c07766
J. Am. Chem. Soc. 2024, 146, 25710−25726

Table 4. Orders of Magnitude (10^x) of χ (Degree of TOF Control) for Each Structure Computed from the Energetic Span Model Using Free Energies Computed from DFT[a]

Alkane\Step	0	I	II‡	III	IV‡	V	VI	VII‡	VIII	IX‡	X	XI
C_2H_6	−5	−6	−1	−3	−2	−4	−4	−5	−4	−3	−9	−3
C_3H_8	−6	−7	−1	−2	−4	−6	−6	−6	−6	−5	−8	−4
i-C_4H_{10}	−8	−8	−1	−3	−3	−14	−11	−6	−7	−4	−5	−6

[a]Table 3, 723 K, 1 bar alkane, 0.01 bar H_2, and 0.001 bar alkene.

As such, the more disparate reactant and product pressures evident for C_2H_6 dehydrogenation reinforces consistency in the relative kinetic-relevance of the two C−H activation steps with the other alkanes.

The selection of entropy treatment to accommodate the inaccuracies of harmonic oscillators (potential source ii) also impacts the resulting free energies, particularly at the relatively high temperatures of alkane dehydrogenation (723 K). These effects are discussed in detail in Supporting Information section S9. The selection of vibrational frequency cutoff for replacement with a fraction of the gas phase entropy (see reaction coordinate diagrams and summary table in Supporting Information section S10) can enable a greater propensity for overestimation of free energies if insufficiently strict (e.g., II‡ and IV‡ are 209 and 250 kJ mol^{-1}, respectively with a cutoff of 50 cm^{-1}). In contrast, estimating the entropy loss as simply 0.3 of the gas phase S_{trans} (irrespective of vibrational frequencies) results in a significant decrease in free energy that favors steps after alkene desorption, resulting in a decrease in free energy of later steps of the reaction coordinate. These results underscore the potential ranges of free energy computed with different approximations for the entropy of surface bound intermediates and TS, with direct implications for discerning the kinetically relevant TS.

To quantitatively evaluate the kinetic significance of each step, we evaluated the energy landscape systematically using the Energetic Span Model.[63] This model uses energies for intermediates and TS to evaluate the energetic states, their relative energies, and the sensitivity of the TOF to changes in the energies to evaluate which species are most abundant on a catalytic surface and which states are TOF-controlling structures. In this model, the TOF of the reaction coordinate is computed by:

$$TOF = \frac{k_B T}{h} \frac{e^{-\Delta G_r/(RT)} - 1}{\sum_{i,j=1}^{N} e^{((T_i - I_j - \delta G_{i,j})/(RT)}} \quad (5)$$

where ΔG_r is the free energy of the reaction, T_i is the energy of TS i, I_j is the energy of intermediate j, N is the number of intermediates and TS, and $\delta G_{i,j}$ is ΔG_r for $i > j$ or 0 if $i < j$. Using the free energies computed for C_3H_8 dehydrogenation (Figure 7, Table 4), the Energetic Span Model predicts a net TOF value of 2000 h^{-1}. This approximation, using free energies determined for approximate reactor conditions (1 bar alkane, 0.01 bar H_2, 0.001 bar alkene) agrees well with those site-normalized forward rates for C_3H_8 dehydrogenation at 723 K and 0.1 bar C_3H_8 (200 h^{-1}, Figure 4), acknowledging first-order kinetics with C_3H_8 pressure and $\eta < 0.1$ for which net rates are slightly smaller. It is cautioned though that the magnitude of the TOF in this model is highly sensitive to the reaction free energy and determined by which side of equilibrium the system resides. As such, the derived TOF values should be used with caution for reactions which are sensitive to the approach to equilibrium. To provide insights into the kinetic relevance of the reaction steps in alkane dehydrogenation, we compare the degree of TOF control (χ) for each step to assess the significance by assessing the derivative of TOF with respect to the energy of each step (E_i):

$$X_{TOF,i} = \left| \frac{1}{TOF} \frac{\delta TOF}{\delta E_i} \right| \quad (6)$$

The results of this analysis, using central difference method, are presented in Table 4 where the order of magnitude of χ (10^X) are shown for each structure for C_2H_6, C_3H_8, and iC_4H_{10}. Larger values (or less negative powers) indicate that the step has a higher degree of TOF control, which can be interpreted as increasing kinetic relevance. As stated previously, ΔG_r has a significant impact on the TOF (step XI) for each alkane, but with decreasing significance for larger alkanes (−3, −4, and −6 for C_2H_6, C_3H_8, and iC_4H_{10}, respectively) where thermodynamics are more favorable for dehydrogenation. The results show that the TOF-determining step for alkane dehydrogenation is generally II‡ (methyl proton abstraction, power of −1 for all alkanes), with IV‡ (β-hydride elimination) having less relevance to kinetic control (powers of −2 to −3). The definitive relevance of II‡ is more evident for larger alkanes, where thermodynamics are less constrained under the conditions of these free energy computations (723 K, 1 bar of C_2H_6, 0.01 bar of H_2, and 0.001 bar). This is further evident by the single order of magnitude difference between II‡ and IV‡ for C_2H_6 dehydrogenation. These results support our designation of proton abstraction from the terminal $-CH_3$ groups as kinetically relevant for C_2H_6, C_3H_8, and iC_4H_{10}.

3.6. Further Considerations to ZrO_2 Active Site Models and Implications on Computed Barriers. In light of the apparent minority of Zr−O pairs as active sites on the catalyst, likely present at edges and corners, and the use of stoichiometric planar surfaces to assess the reaction coordinate, this section considers the adequacy of the specific surface LAB pairs used in this study in describing the most competent active sites for stabilizing TS, in particular for the β-hydride elimination products (species V) that directly influence the TS IV‡ barrier. It also considers the (implausible) involvement of reduced Zr^{3+} centers and the suitability of stoichiometric extended surfaces as structural models.

The β-hydride elimination TS (structure IV‡) is nearly identical in energy and structure to the product state ($\Delta G^{\ddagger}_{723K}$: 212 kJ mol^{-1} for IV‡; ΔG_{723K}: 201 kJ mol^{-1} for V, see Table 3 C_2H_6). This product state consists of a weakly bound alkene interacting with an H^+-H^- pair. Consequently, surfaces (or site structures) that bind this pair more stably would lead to lower activation barriers for β-hydride elimination. The energies of these H^+-H^- pairs were examined over diverse positions at m-$ZrO_2(\bar{1}11)$ surfaces to identify their most stable locations (a visual representation of the local minima for H^- position is included as Figure S17). Among these locations, the

https://doi.org/10.1021/jacs.4c07766
J. Am. Chem. Soc. 2024, 146, 25710−25726

configuration depicted as structure VI (Figure 7) was the most stable one on m-$ZrO_2(\bar{1}11)$ surfaces, indicating that barriers for β-hydride elimination in $IV^{\ddagger}$ are the lowest determined for such structures. Quantum tunneling effects may cause barriers to be lower than DFT-derived values, but they would also affect the proton abstraction first step for which DFT methods give barriers similar to those measured. Tunneling is typically most consequential at near ambient temperatures, where the enthalpic benefits are essential because of inaccessible thermal barriers, and entropy penalties imposed by precise orbital arrangements are less influential in determining free energies (due to low temperatures). They also lead to very large normal kinetic isotope effects (10 − 100),[64] in contrast with the modest C_3H_8/C_3D_8 kinetic isotope effects measured for propane dehydrogenation in this study (k_H/k_D = 2.2).

The computed free energy barrier (1 bar) for the β-hydride elimination TS for C_2H_6 is higher than expected from experimental assessments that indicate that proton abstraction is the sole kinetically relevant step. It was shown above that product pressures and entropy treatments influence these barriers, but such high barriers may also reflect the ZrO_2 surface structure models used, which do not capture the binding properties of Zr−O pairs with lower Zr coordination. Previous studies on m-ZrO_2 have ascribed special reactivity properties to coordinatively unsaturated sites formed either by removal of lattice O-atoms (via treatments in CO[20] or H_2 that form Zr^{3+})[47] or through the formation of structural O-vacancies by substituting Z^{4+} with Ru or Cu atoms.[12] DFT-derived formation energies of O-vacancies on ZrO_2 are extremely high (e.g., 580 kJ mol^{-1} on the 101 lattice plane).[65] Such energies may be lower on edge and corner sites in small nanoparticles (~300 kJ mol^{-1}), but would still require very high temperatures and H_2/H_2O ratios (>10^{22}) unattainable in the contacting fluid. Our computations for the potential reduction of Zr (by Bader charge and density of states, see Supporting Information section S10), refute the presence of reduced Zr species and confirm attributions of reactivity to LAB site pairs at stochiometric surfaces. Treatments in CO (at 823 K) or H_2 (at 823 K) were reported with small rate enhancements (less than 10-fold), contrasting the larger effects reported here after treatments in DME (>100-fold) at much lower temperatures (723 K). The effects of CO are likely to arise from its role as a chemical desiccant (to form CO_2 and H_2, in the analog of water-gas shift reactions); such reactions require higher temperatures than dehydroxylation by DME and they form alternate titrants (CO_2), albeit ones that bind more weakly than H_2O at Zr−O pairs.

The absence and lack of kinetic consequences of Zr^{3+} centers was confirmed by comparing rate enhancements induced by exposing samples to He, H_2 (5 kPa), and DME at 723 K; the first-order dehydrogenation rate constants at 723 K (shown in Figure S9) are about 150 times larger after DME than He or H_2 treatments (which exhibited a similar rate constant of 0.9 times the rate constant after He treatment). Even H_2 treatments at 823 K led to rates comparable to those of He treatments. H_2 uptakes upon treatment of m-ZrO_2 in H_2 up to 893 K (Figure S12) were consistent with H_2 adsorption[66] and much smaller than the measured maximum density of active sites (from H_2O titration, <5.4 μmol g^{-1} or 0.02 H_2 molecules nm^{-2} compared to 0.56 sites nm^{-2}, Figure S2). Impurity Hf species (atomic radii 225 nm) were also considered as sources of active sites due to lattice distortions (Zr radii: 160 nm) and their ubiquitous presence in Zr sources (~2% Hf). Hf was supplemented in the synthesis of zirconate catalysts and was found to have no effect on C_3H_8 dehydrogenation rates, precluding the presence of Hf-induced formation of active LAB site pairs (Supporting Information section S5).

The experimental evidence supports the abstraction of a proton from methyl C−H bonds as the sole kinetically relevant step in alkane dehydrogenation reactions. DFT-derived energies show conclusive agreement with this for light alkane dehydrogenation reactions. C_2H_6 dehydrogenation at standard conditions, however, is less conclusive due to the more similar free energies barriers of the first and second C−H activation steps. Such unequivocal discernment may arise from structural models that are underpinned by direct experimental observations of minority surface structures on polycrystalline ZrO_2 powders.

m-$ZrO_2(\bar{1}11)$ surfaces account for one of several low-index planes exposed at ZrO_2 crystals. H_2O titrations give a quantity of uniquely active sites (0.56 nm^{-2}, Supporting Information section S3) that is much smaller than the number of Zr−O pairs at low index planes of m-ZrO_2 (8−12 nm^{-2}).[67] Sites of lower coordination bind H_2O more strongly and are thus most prone to remain blocked after thermal treatments (titrations data in Supporting Information section S3). Alkane dehydrogenation active site densities on m-ZrO_2 are higher for smaller crystallites[19] which expose a proportionately larger fraction of low-coordination edge and corner sites at surfaces; these features are not inherent in structural models consisting of flat surfaces. Such sites may possess unique geometric arrangements, particularly for the second Zr-atom that is required to stabilize the β-hydride elimination TS, thus preferentially stabilizing this TS over that mediating the first C−H activation step and eliminating any uncertainty in the barrier for TS $IV^{\ddagger}$ for C_2H_6 dehydrogenation. Model low index planar surfaces do not account for steps and kinks that expose low-coordination ZrO_2 on practical catalysts, which directly impact the binding of molecules and potentially the kinetically relevant steps on Zr−O site pairs, making the binding of H^+ and H^- pairs a potential descriptor of reactivity or determining the rate limiting step. Such sites must reflect modest enthalpy barriers of the kinetically relevant TS (84 kJ mol^{-1}) and show the weak binding of surface species that results in the undetectable coverage of alkane derived species in the heterolytic C−H activation that mediates alkane dehydrogenation on LAB site pairs.

4. CONCLUSIONS

Kinetic assessments of alkane dehydrogenation rates on m-ZrO_2, made possible by DME cleaning protocols to expose the active Lewis acid−base pairs, were used in conjunction with theoretical modeling of the reaction pathway on a simulated m-ZrO_2 surface. The data and mechanistic analysis show that dehydrogenation of C_2H_6, C_3H_8, nC_4H_{10}, and iC_4H_{10} involves kinetically relevant cleavage of terminal C−H bonds via unimolecular transition states stabilized by interactions with Zr−O LAB site pairs that remain essentially uncovered during steady-state catalysis. The heterolytic C−H bond activation forms a surface-stabilized carbanion and proton pair that undergoes subsequent β-hydride abstraction to form the product alkene and H_2. The predicted barriers for the first proton abstraction step for each alkane are similar, consistent with measured barriers for dehydrogenation among alkanes

https://doi.org/10.1021/jacs.4c07766
J. Am. Chem. Soc. 2024, 146, 25710−25726

(84 kJ mol^{-1}). Differences in the heterolytic dehydrogenation reactivity of alkanes arise from differences in the entropy of activation for each molecule, apparently due to larger residual mobility of adsorbed alkane-derived species with longer, or more, fragments which are not directly bound to the surface. These fragments retain mobility, resulting in higher dehydrogenation rate constants. LAB active site pairs on *m*-ZrO_2 that activate C−H bonds in alkane molecules represent only a small fraction of surface Zr−O pairs and are ascribed to the low-coordination edge and corner sites. The reactivity of *m*-ZrO_2 is invariant to reductive treatments, given the nonreducible nature of ZrO_2, but is strongly dependent on the crystallite size. This work discloses mechanistic assessment for heterolytic C−H activation on the LAB site pairs of a *m*-ZrO_2 whose active Zr−O site pairs have been uncovered of dissociatively bound H_2O by chemical treatments with dimethyl ether to exhibit alkane dehydrogenation rates comparable to those of commercial Cr- and Pt-based catalysts. Based on these findings, further research focusing on the controlled formation of active and stable LAB site pairs in zirconia or other metal oxide materials holds significant potential in terms of replacing toxic and expensive metals with more abundant alternatives.

■ ASSOCIATED CONTENT

Supporting Information

The Supporting Information is available free of charge at https://pubs.acs.org/doi/10.1021/jacs.4c07766.

Surface area assessments; X-ray diffraction; active site titrations by H_2O; additional supporting data; synthesis of Hf-doped ZrO_2; H_2 temperature programmed reduction; calculation of enthalpies and entropies using statistical mechanics formalisms; reaction coordinate at differing reaction conditions; sensitivity of the reaction coordinate on selection of entropy treatments; supporting computational data; DFT-optimized atomic coordinates (PDF)

■ AUTHOR INFORMATION

Corresponding Author

Enrique Iglesia − *Department of Chemical and Biomolecular Engineering, University of California at Berkeley, Berkeley, California 94720, United States; Davidson School of Chemical Engineering, Purdue University, West Lafayette, Indiana 47907, United States;* orcid.org/0000-0003-4109-1001; Email: iglesia@berkeley.edu

Authors

Nicholas R. Jaegers − *Department of Chemical and Biomolecular Engineering, University of California at Berkeley, Berkeley, California 94720, United States;* orcid.org/0000-0002-9930-7672

Vardan Danghyan − *Department of Chemical and Biomolecular Engineering, University of California at Berkeley, Berkeley, California 94720, United States*

Junnan Shangguan − *Department of Chemical and Biomolecular Engineering, University of California at Berkeley, Berkeley, California 94720, United States*

Carlos Lizandara-Pueyo − *BASF SE, 67056 Ludwigshafen am Rhein, Germany;* orcid.org/0000-0003-1146-775X

Prashant Deshlahra − *Department of Chemical and Biological Engineering, Tufts University, Medford, Massachusetts 02155, United States;* orcid.org/0000-0002-1063-4379

Complete contact information is available at: https://pubs.acs.org/10.1021/jacs.4c07766

Notes

The authors declare the following competing financial interest(s): The authors have filed provisional patent applications for the catalyst compositions and methods of preparation and pretreatment protocols of metal oxides for alkane dehydrogenation reactions.

■ ACKNOWLEDGMENTS

We acknowledge BASF for financial support and technical guidance through the California Research Alliance. This research used resources of the National Energy Research Scientific Computing Center (NERSC), a U.S. Department of Energy Office of Science User Facility located at Lawrence Berkeley National Laboratory, operated under Contract No. DE-AC02-05CH11231 using NERSC award ERCAP0023779. The authors acknowledge Dr. Gregory Tate for restoring the Quantasorb QS-10 used in TPR experiments.

■ REFERENCES

(1) Agarwal, A.; Sengupta, D.; El-Halwagi, M. Sustainable Process Design Approach for on-Purpose Propylene Production and Intensification. *ACS Sustainable Chem. Eng* **2018**, *6*, 2407−2421.

(2) Chen, S.; et al. Propane Dehydrogenation on Single-Site [$PtZn_4$] Intermetallic Catalysts. *Chem-Us* **2021**, *7*, 387−405.

(3) Soraker, P.; Jensen, S.; Rytter, E.; Ronnekleiv, M. Pretreatment of a Pt/Sn-Based Catalyst. EP 1 206 319 A1, 2002.

(4) Zimmermann, H.; Versluis, F. Process and Catalyst for Dehydrogenation or Dehydrocyclization of Hydrocarbons. US5378350A, 1995.

(5) Conley, M. P.; Delley, M. F.; Núñez-Zarur, F.; Comas-Vives, A.; Copéret, C. Heterolytic Activation of C−H Bonds on Cr^{III}-O Surface Sites Is a Key Step in Catalytic Polymerization of Ethylene and Dehydrogenation of Propane. *Inorg. Chem.* **2015**, *54*, 5065−5078.

(6) Chen, S.; Chang, X.; Sun, G.; Zhang, T.; Xu, Y.; Wang, Y.; Pei, C.; Gong, J. Propane Dehydrogenation: Catalyst Development, New Chemistry, and Emerging Technologies. *Chem Soc Rev* **2021**, *50*, 3315−3354.

(7) Wang, W.; et al. Single Co Sites in Ordered SiO_2 Channels for Boosting Nonoxidative Propane Dehydrogenation. *ACS Catal.* **2022**, *12*, 2632−2638.

(8) Wu, L.; Ren, Z.; He, Y.; Yang, M.; Yu, Y.; Liu, Y.; Tan, L.; Tang, Y. Atomically Dispersed Co^{2+} Sites Incorporated into a Silicalite-1 Zeolite Framework as a High-Performance and Coking-Resistant Catalyst for Propane Nonoxidative Dehydrogenation to Propylene. *ACS Appl. Mater. Interfaces* **2021**, *13*, 48934−48948.

(9) Hu, B.; Kim, W.-G.; Sulmonetti, T. P.; Sarazen, M. L.; Tan, S.; So, J.; Liu, Y.; Dixit, R. S.; Nair, S.; Jones, C. W. A Mesoporous Cobalt Aluminate Spinel Catalyst for Nonoxidative Propane Dehydrogenation. *Chemcatchem* **2017**, *9*, 3330−3337.

(10) Searles, K.; Siddiqi, G.; Safonova, O. V.; Copéret, C. Silica-Supported Isolated Gallium Sites as Highly Active, Selective and Stable Propane Dehydrogenation Catalysts. *Chem. Sci.* **2017**, *8*, 2661−2666.

(11) Cybulskis, V. J.; Pradhan, S. U.; Lovón-Quintana, J. J.; Hock, A. S.; Hu, B.; Zhang, G.; Delgass, W. N.; Ribeiro, F. H.; Miller, J. T. The Nature of the Isolated Gallium Active Center for Propane Dehydrogenation on Ga/Sio_2. *Catal. Lett.* **2017**, *147*, 1252−1262.

(12) Otroshchenko, T.; Sokolov, S.; Stoyanova, M.; Kondratenko, V. A.; Rodemerck, U.; Linke, D.; Kondratenko, E. V. ZrO_2-Based Alternatives to Conventional Propane Dehydrogenation Catalysts: Active Sites, Design, and Performance. *Angew. Chem., Int. Ed.* **2015**, *54*, 15880−15883.

(13) Tanabe, K. Surface and Catalytic Properties of ZrO_2. *Mater. Chem. Phys.* **1985**, *13*, 347−364.

(14) Tanabe, K.; Yamaguchi, T. Acid-Base Bifunctional Catalysis by ZrO_2 and Its Mixed Oxides. *Catal. Today* **1994**, *20*, 185−197.
(15) Radha, A.; Bomati-Miguel, O.; Ushakov, S. V.; Navrotsky, A.; Tartaj, P. Surface Enthalpy, Enthalpy of Water Adsorption, and Phase Stability in Nanocrystalline Monoclinic Zirconia. *J. Am. Ceram. Soc.* **2009**, *92*, 133−140.
(16) Lackner, P.; Hulva, J.; Köck, E.-M.; Mayr-Schmölzer, W.; Choi, J. I. J.; Penner, S.; Diebold, U.; Mittendorfer, F.; Redinger, J.; Klötzer, B.; et al. Water Adsorption at Zirconia: From the ZrO_2 (111)/Pt_3Zr(0001) Model System to Powder Samples. *J. Mater. Chem. A* **2018**, *6*, 17587−17601.
(17) Korhonen, S. T.; Calatayud, M.; Krause, A. O. I. Stability of Hydroxylated (111) and (101) Surfaces of Monoclinic Zirconia: A Combined Study by DFT and Infrared Spectroscopy. *J. Phys. Chem. C* **2008**, *112*, 6469−6476.
(18) Iglesia, E.; Shangguan, J. Pre-Treating Metal Oxide Catalysts for Alkane Dehydrogenation. 20230303465, 2022.
(19) Danghyan, V.; Jaegers, N.; Lizandara-Pueyo, C.; Cain-Borgman, C.; Dellamorte, J.; Kundu, A.; Shangguan, J.; Iglesia, E. Lewis Acid Base Pairs as Highly Active Catalytic Sites for Hydrogenation and Dehydrogenation Processes. 2024016500, 2023.
(20) Zhang, Y.; Zhao, Y.; Otroshchenko, T.; Lund, H.; Pohl, M.-M.; Rodemerck, U.; Linke, D.; Jiao, H.; Jiang, G.; Kondratenko, E. V. Control of Coordinatively Unsaturated Zr Sites in ZrO_2 for Efficient C−H Bond Activation. *Nat. Commun.* **2018**, *9*, 3794.
(21) Li, W.; Huang, H.; Li, H.; Zhang, W.; Liu, H. Facile Synthesis of Pure Monoclinic and Tetragonal Zirconia Nanoparticles and Their Pahse Effects on the Behavior of Supported Molybdena Catalysts for Methanol Seletive Oxidation. *Langmuir* **2008**, *24*, 8358−8366.
(22) Price, G. L.; Iglesia, E. Matrix-Method for Correction of Mass-Spectra in Deuterium-Exchange Applications. *Ind. Eng. Chem. Res.* **1989**, *28*, 839−844.
(23) Kresse, G.; Furthmuller, J. Efficient Iterative Schemes for Ab Initio Total-Energy Calculations Using a Plane-Wave Basis Set. *Phys. Rev. B* **1996**, *54*, 11169−11186.
(24) Perdew, J. P.; Burke, K.; Ernzerhof, M. Generalized Gradient Approximation Made Simple. *Phys. Rev. Lett.* **1996**, *77*, 3865−3868.
(25) Grimme, S.; Antony, J.; Ehrlich, S.; Krieg, H. A Consistent and Accurate Ab Initio Parametrization of Density Functional Dispersion Correction (DFT-D) for the 94 Elements H-Pu. *J. Chem. Phys.* **2010**, *132*, 154104.
(26) Kresse, G.; Joubert, D. From Ultrasoft Pseudopotentials to the Projector Augmented-Wave Method. *Phys. Rev. B* **1999**, *59*, 1758.
(27) Jaegers, N. R.; Iglesia, E. Theoretical Assessment of the Mechanism and Active Sites in Alkene Dimerization on Ni Monomers Grafted onto Aluminosilicates: $(Ni\text{-}OH)^+$ Centers and C-C Coupling Mediated by Lewis Acid-Base Pairs. *J. Am. Chem. Soc.* **2023**, *145*, 6349−6361.
(28) Monkhorst, H. J.; Pack, J. D. Special Points for Brillouin-Zone Integrations. *Phys. Rev. B* **1976**, *13*, 5188−5192.
(29) Henkelman, G.; Jonsson, H. Improved Tangent Estimate in the Nudged Elastic Band Method for Finding Minimum Energy Paths and Saddle Points. *J. Chem. Phys.* **2000**, *113*, 9978−9985.
(30) Henkelman, G.; Uberuaga, B. P.; Jónsson, H. A Climbing Image Nudged Elastic Band Method for Finding Saddle Points and Minimum Energy Paths. *J. Chem. Phys.* **2000**, *113*, 9901−9904.
(31) Henkelman, G.; Jónsson, H. A Dimer Method for Finding Saddle Points on High Dimensional Potential Surfaces Using Only First Derivatives. *J. Chem. Phys.* **1999**, *111*, 7010−7022.
(32) McQuarrie, D. In *Statistical Mechanics*; University Science Books: Sausalito, CA, 2000; pp 222−223.
(33) Sprowl, L. H.; Campbell, C. T.; Árnadóttir, L. Hindered Translator and Hindered Rotor Models for Adsorbates: Partition Functions and Entropies. *J. Phys. Chem. C* **2016**, *120*, 9719−9731.
(34) Deshlahra, P.; Iglesia, E. Methanol Oxidative Dehydrogenation on Oxide Catalysts: Molecular and Dissociative Routes and Hydrogen Addition Energies as Descriptors of Reactivity. *J. Phys. Chem. C* **2014**, *118*, 26115−26129.
(35) Deshlahra, P.; Iglesia, E. Reactivity and Selectivity Descriptors for the Activation of C−H Bonds in Hydrocarbons and Oxygenates on Metal Oxides. *J. Phys. Chem. C* **2016**, *120*, 16741−16760.
(36) Johnson, R. D. NIST Standard Reference Database Number 101. In *NIST Computational Chemistry Comparison and Benchmark Database*, 2022. http://cccbdb.nist.gov/ (accessed 2022−04−04).
(37) Cramer, C. J. In *Essentials of Computational Chemistry: Theories and Models*; Wiley, 2005: p 618.
(38) Wang, S.; Iglesia, E. Substituent Effects and Molecular Descriptors of Reactivity in Condensation and Esterification Reactions of Oxygenates on Acid-Base Pairs at TiO_2 and ZrO_2 Surfaces. *The Journal of Physical Chemistry C* **2016**, *120*, 21589−21616.
(39) Jain, A.; Ong, S. P.; Hautier, G.; Chen, W.; Richards, W. D.; Dacek, S.; Cholia, S.; Gunter, D.; Skinner, D.; Ceder, G.; et al. Commentary: The Materials Project: A Materials Genome Approach to Accelerating Materials Innovation. *APL Mater.* **2013**, *1*, 011002.
(40) Monkhorst, H. J.; Pack, J. D. Special Points for Brillouin-Zone Integrations. *Phys. Rev. B* **1976**, *13*, 5188.
(41) Zhang, Y.; Zhao, Y.; Otroshchenko, T.; Han, S.; Lund, H.; Rodemerck, U.; Linke, D.; Jiao, H.; Jiang, G.; Kondratenko, E. V. The Effect of Phase Composition and Crystallite Size on Activity and Selectivity of ZrO_2 in Non-Oxidative Propane Dehydrogenation. *J. Catal.* **2019**, *371*, 313−324.
(42) Wu, H.; Duan, Y.; Liu, K.; Lv, D.; Qin, L.; Shi, L.; Tang, G. First-Principles Study of Phase Transition and Band Structure of ZrO_2 under Pressure. *J. Alloys Compd.* **2015**, *645*, 352−357.
(43) Hofmann, A.; Sauer, J. Surface Structure of Hydroxylated and Sulfated Zirconia. A Periodic Density-Functional Study. *J. Phys. Chem. B* **2004**, *108*, 14652−14662.
(44) French, R. H.; Glass, S.; Ohuchi, F.; Xu, Y.-N.; Ching, W. Experimental and Theoretical Determination of the Electronic Structure and Optical Properties of Three Phases of ZrO_2. *Phys. Rev. B* **1994**, *49*, 5133.
(45) Howard, C.; Hill, R.; Reichert, B. Structures of ZrO_2 Polymorphs at Room Temperature by High-Resolution Neutron Powder Diffraction. *Acta Crystallogr., Sect. B: Struct. Sci.* **1988**, *44*, 116−120.
(46) Ruh, R.; Corfield, P. W. Crystal Structure of Monoclinic Hafnia and Comparison with Monoclinic Zirconia. *J. Am. Ceram. Soc.* **1970**, *53*, 126−129.
(47) Zhang, Y.; Zhao, Y.; Otroshchenko, T.; Lund, H.; Pohl, M.-M.; Rodemerck, U.; Linke, D.; Jiao, H.; Jiang, G.; Kondratenko, E. V. Control of Coordinatively Unsaturated Zr Sites in ZrO_2 for Efficient C−H Bond Activation. *Nat. Commun.* **2018**, *9*, 3794.
(48) Hofmann, A.; Clark, S. J.; Oppel, M.; Hahndorf, I. Hydrogen Adsorption on the Tetragonal ZrO_2 (101) Surface: A Theoretical Study of an Important Catalytic Reactant. *Phys. Chem. Chem. Phys.* **2002**, *4*, 3500−3508.
(49) Haase, F.; Sauer, J. The Surface Structure of Sulfated Zirconia: Periodic Ab Initio Study of Sulfuric Acid Adsorbed on ZrO_2 (101) and ZrO_2 (001). *J. Am. Chem. Soc.* **1998**, *120*, 13503−13512.
(50) Christensen, A.; Carter, E. A. First-Principles Study of the Surfaces of Zirconia. *Phys. Rev. B* **1998**, *58*, 8050.
(51) Morterra, C.; Cerrato, G.; Ferroni, L.; Negro, A.; Montanaro, L. Surface Characterization of Tetragonal ZrO_2. *Appl. Surf. Sci.* **1993**, *65*, 257−264.
(52) Momma, K.; Izumi, F. Vesta 3 for Three-Dimensional Visualization of Crystal, Volumetric and Morphology Data. *J. Appl. Crystallogr.* **2011**, *44*, 1272−1276.
(53) Xu, M.; Lunsford, J. H.; Goodman, D. W.; Bhattacharyya, A. Synthesis of Dimethyl Ether (DME) from Methanol over Solid-Acid Catalysts. *Applied Catalysis A: General* **1997**, *149*, 289−301.
(54) Takeishi, K.; Suzuki, H. Steam Reforming of Dimethyl Ether. *Appl. Catal., A* **2004**, *260*, 111−117.
(55) Vu, B. K.; Song, M. B.; Ahn, I. Y.; Suh, Y.-W.; Suh, D. J.; Kim, W.-I.; Koh, H.-L.; Choi, Y. G.; Shin, E. W. Pt-Sn Alloy Phases and Coke Mobility over Pt-Sn/Al_2O_3 and Pt-Sn/$ZnAl_2O_4$ Catalysts for Propane Dehydrogenation. *Appl. Catal., A* **2011**, *400*, 25−33.

https://doi.org/10.1021/jacs.4c07766
J. Am. Chem. Soc. 2024, 146, 25710−25726

(56) Voskoboynikov, T. V.; Wei, D. H.; Sachtler, J. W. A.; Vora, B. V. Dehydrogenation Catalyst Composition. US6756340B2, 2002.
(57) Luo, Y.-R. *Comprehensive Handbook of Chemical Bond Energies*; CRC Press: New York, 2007.
(58) Campbell, C. T.; Sellers, J. R. V. The Entropies of Adsorbed Molecules. *J. Am. Chem. Soc.* **2012**, *134*, 18109−18115.
(59) Flaherty, D. W.; Iglesia, E. Transition-State Enthalpy and Entropy Effects on Reactivity and Selectivity in Hydrogenolysis of *n*-Alkanes. *J. Am. Chem. Soc.* **2013**, *135*, 18586−18599.
(60) Onishi, T.; Abe, H.; Maruya, K.-i.; Domen, K. I.R. Spectra of Hydrogen Adsorbed on ZrO_2. *J. Chem. Soc., Chem. Commun.* **1985**, 617−618.
(61) Nakatsuji, H.; Hada, M.; Ogawa, H.; Nagata, K.; Domen, K. Theoretical Study on the Molecular and Dissociative Adsorptions of H_2 on a ZrO_2 Surface. *J. Phys. Chem.* **1994**, *98*, 11840−11845.
(62) Jaegers, N.; Hense, J.; Shangguan, J.; Deshlahra, P.; Iglesia, E. Heterolytic Activation of H-H and H-OH Bonds on Lewis Acid-Base Site Pairs of Metal Oxides: Impact of Geometry and through-Space Interactions on Brønsted-Evans-Polanyi Scaling Relations, 2024, in preparation.
(63) Kozuch, S.; Shaik, S. How to Conceptualize Catalytic Cycles? The Energetic Span Model. *Acc. Chem. Res.* **2011**, *44*, 101−110.
(64) Klinman, J. P.; Kohen, A. Hydrogen Tunneling Links Protein Dynamics to Enzyme Catalysis. *Annu. Rev. Biochem.* **2013**, *82*, 471−496.
(65) Ruiz Puigdollers, A.; Schlexer, P.; Tosoni, S.; Pacchioni, G. Increasing Oxide Reducibility: The Role of Metal/Oxide Interfaces in the Formation of Oxygen Vacancies. *ACS Catal.* **2017**, *7*, 6493−6513.
(66) Hoang, D.; Lieske, H. Effect of Hydrogen Treatments on ZrO_2 and Pt/ZrO_2 Catalysts. *Catal. Lett.* **1994**, *27*, 33−42.
(67) Piskorz, W.; Gryboś, J.; Zasada, F.; Cristol, S.; Paul, J.-F.; Adamski, A.; Sojka, Z. Periodic Dft and Atomistic Thermodynamic Modeling of the Surface Hydration Equilibria and Morphology of Monoclinic ZrO_2 Nanocrystals. *J. Phys. Chem. C* **2011**, *115*, 24274−24286.

https://doi.org/10.1021/jacs.4c07766
J. Am. Chem. Soc. 2024, 146, 25710−25726